Harnessing AlphaFold to reveal hERG channel conformational state secrets

Khoa Ngo*[1,2], Pei-Chi Yang [1,2], Vladimir Yarov-Yarovoy[1,2,3], Colleen E. Clancy*[1,2,4], Igor Vorobyov*[2,4]

[1]*Center for Precision Medicine and Data Science,*
[2]*Department of Physiology and Membrane Biology,*
[3]*Department of Anesthesiology and Pain Medicine,*
[4]*Department of Pharmacology,*
University of California, Davis, California

*Corresponding authors

Email: khoango@ucdavis.edu, ceclancy@ucdavis.edu, ivorobyov@ucdavis.edu

Short title: AlphaFold application to reveal hERG channel states

Author Contributions: K.N. designed the research study, conducted simulations, acquired data, analyzed data, and wrote the manuscript. P.-C.Y., V.Y.-Y., C.E.C., and I.V. designed the research study, analyzed data, and wrote the manuscript.

Competing Interest Statement: The authors declare no competing interests.

Classification: Structural Biology and Molecular Biophysics, Biochemistry and Chemical Biology

Keywords: Voltage-gated potassium channel, hERG, AlphaFold, molecular docking, molecular dynamics simulation

Abstract

To design safe, selective, and effective new therapies, there must be a deep understanding of the structure and function of the drug target. One of the most difficult problems to solve has been resolution of discrete conformational states of transmembrane ion channel proteins. An example is $K_V11.1$ (hERG), comprising the primary cardiac repolarizing current, I_{Kr}. hERG is a notorious drug anti-target against which all promising drugs are screened to determine potential for arrhythmia. Drug interactions with the hERG inactivated state are linked to elevated arrhythmia risk, and drugs may become trapped during channel closure. However, the structural details of multiple conformational states have remained elusive. Here, we guided AlphaFold2 to predict plausible hERG inactivated and closed conformations, obtaining results consistent with multiple available experimental data. Drug docking simulations demonstrated hERG state-specific drug interactions in good agreement with experimental results, revealing that most drugs bind more effectively in the inactivated state and are trapped in the closed state. Molecular dynamics simulations demonstrated ion conduction for an open but not AlphaFold2 predicted inactivated state that aligned with earlier studies. Finally, we identified key molecular determinants of state transitions by analyzing interaction networks across closed, open, and inactivated states in agreement with earlier mutagenesis studies. Here, we demonstrate a readily generalizable application of AlphaFold2 as an effective and robust method to predict discrete protein conformations, reconcile seemingly disparate data and identify novel linkages from structure to function.

Introduction

Understanding the dynamic conformational changes of proteins is fundamental to elucidating their functions, interactions, and roles in biological processes. Many proteins, especially membrane proteins that constitute a significant portion of drug targets, exist in multiple functionally distinct states. Capturing these various conformations is crucial for predicting how proteins interact with ligands, designing drugs that selectively target specific states, and uncovering the mechanisms that regulate these interactions. However, experimental techniques like cryo-electron microscopy (cryo-EM) often provide only static snapshots of proteins, typically capturing a single conformational state due to experimental constraints. Computational methods such as molecular dynamics simulations can sample alternative conformations but are limited by timescales and computational resources, often failing to observe meaningful conformational changes that result in functional effects. Enhanced sampling simulation techniques can help extend the timescales, but the biasing factors introduced to accelerate the simulations can sometimes push proteins into non-physiological conformations, potentially skewing the accuracy of the predictions and limiting their biological relevance.

Recent advances in deep learning have revolutionized protein structure prediction, with tools like AlphaFold2 (Jumper et al., 2021a) achieving remarkable success in predicting protein structures based on amino acid sequences. However, conventional applications of these AI-based methods often result in the prediction of a single, static conformation, akin to experimental snapshots. This raises a significant question: *Can we harness the capabilities of artificial intelligence to predict different physiologically relevant conformations of proteins, thereby capturing the dynamic spectrum of states essential for understanding protein function and drug interactions?*

To address this question, we employed and validated different strategies to guide AlphaFold2 to predict multiple physiologically relevant conformations, surpassing the usual single-state predictions. As a proof of concept, we applied this approach to the human voltage-gated potassium channel $K_V11.1$, encoded by the KCNH2 or human Ether-à-go-go-Related Gene (hERG) gene, a well-known drug anti-target in pharmacology and cardiology due to its role in drug-induced arrhythmias. hERG is a key player in cardiac electrophysiology, underpinning the rapid component of the delayed rectifier K^+ current (I_{Kr}) in cardiac myocytes (Vandenberg et al., 2012). This current plays a crucial role in the repolarization phase of the cardiac action potential (Sanguinetti and Tristani-Firouzi, 2006). Perturbation to hERG channel function, resulting from genetic anomalies or pharmacological interventions, can precipitate multiple arrhythmogenic disorders (Sanguinetti and Tristani-Firouzi, 2006).

The hERG channel is a homotetramer, with each subunit containing six membrane-spanning segments (S1-S6) (Wang and MacKinnon, 2017). The segments S5 and S6 along with the intervening loops and pore helix form the channel pore domain (PD), crucial for potassium ion passage along the central pore, while segments S1-S4 form the voltage sensing domain (VSD), responding to voltage changes across the cell membrane. Notably, the hERG channel also features specialized intracellular regions: the Per-Arnt-Sim (PAS) domain at the N-terminus and the cyclic nucleotide-binding domain (CNBD) at the C-terminus.

The distinctive pharmacological promiscuity of the hERG channel makes it prone to blockade by a diverse array of drugs, creating cardiac safety pharmacology risk in the drug discovery process. Blockade of the hERG channel by drugs can lead to QT interval prolongation known as an acquired long QT syndrome (aLQTS) and escalate the risk of *torsades de pointes* (TdP), a potentially fatal arrhythmia (Li and Ramos, 2017). This issue has prompted the withdrawal of various drugs from the market and underscored the necessity of incorporating hERG safety evaluations in the drug development pipeline (Ferri et al., 2013; Kocadal et al., 2018; Waldo et al., 1996). The susceptibility for drug blockade is not uniform but varies depending on the channel conformational state, a phenomenon known as state-dependent drug block. Drugs may preferentially bind to and block the channel in specific states (open, closed, or inactivated), which can differentially affect cardiac repolarization and rhythm (Perrin et al., 2008; Priest et al., 2008) and thus confer different risks for aLQTS and TdP arrhythmias as shown in our previous study (Yang et al., 2020).

However, capturing the dynamic spectrum of hERG channel states poses a formidable challenge. While cryo-electron microscopy (cryo-EM) has offered invaluable insights into the putative open state of the channel (Asai et al., 2021; Wang and MacKinnon, 2017), a comprehensive view of the closed and inactivated states has remained elusive. Thus, even as we embark on a scientific era of explosive growth fueled by the convergence of protein

2

structure insights, computational capabilities, and artificial intelligence (AI) based modeling and synthetic data, the next frontier is marked by the need to reveal all relevant conformational states of proteins. The existing knowledge gaps constrain both predictive capabilities regarding drug – protein interactions and the creation of therapies through drug discovery to find specific and selective drugs, or in the case of hERG, to minimize their adverse interactions. For example, our recent study by Yang *et al.* introduced a multiscale model framework to forecast drug-induced cardiotoxicity at cellular and tissue levels, utilizing atomistic simulations of drug interactions with the hERG channel (Yang et al., 2020). However, the absence of hERG structural models in the inactivated and closed states limited the predictive potential of atomistic scale simulations of state-specific drug binding.

The emergence of AlphaFold2, a protein structure prediction tool driven by machine learning, has brought a paradigm shift in structural biology (Jumper et al., 2021a). AlphaFold2 represents a significant advance over previous methods by using deep learning to predict the three-dimensional structures of proteins based purely on their amino acid sequences (Jumper et al., 2021a). AlphaFold2 primarily requires the amino acid sequence of a protein as its input, but the method utilizes other key elements: in addition to the amino acid sequence, AlphaFold2 can also utilize multiple sequence alignments (MSAs) of similar sequences from different species, templates of related protein structures when available, and/or homologous proteins (Jumper et al., 2021a). Evolutionarily conserved regions over multiple isoforms and species indicated that the sequence is crucial for structural integrity. These additional inputs help the model to identify evolutionary and structural constraints that are crucial for accurate predictions. The output of AlphaFold2 is a predicted 3D structure of the protein that includes inter-residue distance predictions, whereby the model predicts the distances between every pair of amino acid residues in the protein. Predictions about the angles between bonds that connect amino acid residues are also generated as angle predictions that are crucial for determining the precise shape of the protein fold.

AlphaFold2's limitation, in its default configuration, is that it generates only a single-state structure (Lane, 2023), which for the hERG channel corresponds to the open state. In this study, we introduced an easily replicable and generally applicable approach to guide AlphaFold2 in predicting multiple, physiologically relevant conformations of proteins. By employing multiple structural templates and refining input parameters, we enhanced the predictive capabilities of AlphaFold2, enabling it to generate highly relevant and physically plausible protein conformations beyond the default single-state prediction. We conducted drug docking simulations to predict how specific drugs interact with the hERG channel in different conformational states and performed molecular dynamics simulations to assess ion conduction across these states. Throughout the process, we validated our predictions by comparing them with experimental data, ensuring that both the drug interactions and ion conductive properties aligned with observed experimental outcomes. This method opens new possibilities for *in silico* studies of protein dynamics, drug design, and safety assessments, allowing researchers to explore the full range of conformational states that proteins may adopt.

Results

Generating hERG channel conformational states

It well known that the hERG channel resides in discrete functional states, minimally comprising closed, open, and inactivated states, which interconnect as a function of time and membrane voltage (Vandenberg et al., 2012). In the open state, the channel conducts K^+ ions through a central pore. In contrast, the closed and inactivated states are non-conductive due to either a constricted pore at the intracellular gate (closed state) or a distorted selectivity filter (inactivated state) (Vandenberg et al., 2012). So far, published experimental cryo-EM structures resolved the channel in an open state (Asai et al., 2021; Wang and MacKinnon, 2017). Starting with the experimental structure, computational studies explored hERG inactivation by simulating how different membrane voltages can change the selectivity filter and thus affect ion conduction through the channel (Li et al., 2021; Miranda et al., 2020; Yang et al., 2020). These studies are essential but have some limitations, as the high voltages applied can force the channel into unnatural conformations, and the simulations are not long enough to allow observation of state transitions (Shi

3

et al., 2020). To overcome these limitations, we adopted different modeling strategies to guide AlphaFold2 in producing diverse conformations relevant to specific functional states of the hERG channel.

The first modeling strategy involves using a structural fragment from an experimental structure of a homologous protein that exhibits the desired characteristics of the target state we aim to model in our channel. This fragment serves as a structural template, and AlphaFold2 is used to rebuild the rest of the channel while adhering to the constraints of the template. For example, to model the closed state of the hERG channel, it is known that channel closure requires the voltage sensor in the voltage-sensing domain to be in a deactivated conformation. To achieve this, we used the deactivated voltage-sensing domain from the closed-state rat EAG channel cryo-EM structure (PDB 8EP1, residues H208 – H343) (Mandala and MacKinnon, 2022) and combined it with the selectivity filter from the open-state hERG cryo-EM structure (PDB 5VA2, residues I607 – T634) (Wang and MacKinnon, 2017). This hybrid structure was used as the template for AlphaFold2 predictions, as illustrated in **Figure 1a**. Using these discrete structural fragments, AlphaFold2 was then applied to generate 100 models, specifically configured to encourage diverse prediction outcomes for further analysis.

For modeling the open hERG channel state, we utilized the existing cryo-EM structure of hERG (PDB 5VA2) (Wang and MacKinnon, 2017) and rebuilt the missing extracellular loops using the Rosetta (Fleishman et al., 2011) with the results shown in **Figure 1b**. This reconstructed model served as a basis for molecular dynamics and drug docking simulations.

The second modeling strategy addresses situations where structural information about state transitions is either limited or inconsistent. In this approach, we erase regions – expected to undergo changes during state transition – from an existing structure and use AlphaFold2 to sample potential conformations for these regions. The predictions are evaluated using standard accuracy metrics to ensure their physical plausibility. This allows AlphaFold2 to identify possible substates, which are then grouped into clusters of structurally similar models for further analysis. For example, during hERG inactivation, the selectivity filter shifts from an open, conductive to a distorted, non-conductive conformation, as shown by numerous studies on hERG and other K^+ channels (Butler et al., 2020; Cuello et al., 2010; Fan et al., 1999; Li et al., 2021; Pettini et al., 2023; Schönherr and Heinemann, 1996; Tan et al., 2022; Wu et al., 2023). Moreover, there are a number of studies that do not uniformly suggest a single discrete structure of the inactivated state selectivity filter but propose several alternative conformations (Lau et al., 2024; Li et al., 2021).

To model the inactivated state of hERG, first we configured AlphaFold2 to introduce more uncertainty into the sampling process. As illustrated in **Figure 1c**, starting with the open state cryo-EM structure (PDB 5VA2) (Wang and MacKinnon, 2017), we removed everything except for the cytosolic domain (S660 – R863), then let AlphaFold2 reconstruct the transmembrane domain. In half of the resulting predictions, including the top-ranked model by prediction confidence, the selectivity filter showed a distinct lateral flip of the backbone carbonyl oxygens at residue V625 compared to the open-state structure. This flip created a potential barrier that could prevent K^+ ions from crossing between the S3 and S2 ion-binding sites. To further investigate this conformation, we extracted the predicted selectivity filter region (residues Y607 – T634) and merged them with the activated VSDs (W398 – V549) and the cytosolic domain (S660 – R863) from the open-state hERG structure (PDB 5VA2) (Wang and MacKinnon, 2017) to create a new structural template. Then, we generated 100 more models for further analysis.

Clustering of AlphaFold2-generated hERG models reveals predominant substates

A key distinction of our approach is that, rather than relying solely on single-model predictions, we generated a diverse population of models to better explore the conformational landscape. By clustering these models, we identified predominant substates, represented as clusters of structurally similar models. To determine which of these substates are likely to be physiologically relevant, we quantitatively assessed the structural reliability within each cluster using the predicted Local Distance Difference Test (pLDDT). Higher pLDDT scores indicate more

4

reliable and accurate structural predictions (Jumper et al., 2021a). This clustering approach helps to capture a range of conformations that might represent stable states of the protein.

For each predicted conformational state of hERG, we clustered 100 predicted structural models based by their degree of similarity, quantified by the root-mean-square deviation (RMSD), as shown in **Figure 2**.

Closed-state clusters: The analysis of closed-state clusters showed only minor differences in RMSD and pLDDT values between them. When comparing the top-ranked models from each cluster, the all-atom RMSD between cluster 1 (the cluster with the highest confidence) and cluster 2 was just 0.36 Å, while the RMSD between cluster 1 and the outlier cluster was 0.95 Å. (Outlier clusters are those with fewer than three members.) This indicates small structural differences among the models. Aside from the outlier cluster, the average pLDDT scores for clusters 1 and 2 were also very similar. The low RMSD values suggest that the predictions are converging on a similar overall conformation, with the minor differences likely due to slight variations in the positioning of the intracellular loop regions. As a result, the top-ranked model from cluster 1 **(Figure 2b)** was selected for further simulations.

Inactivated-state clusters: As inactivation is known to affect the selectivity filter (SF), we grouped the models by focusing exclusively on similarity of the selectivity filter (S624 – G628) conformations. We ranked the clusters according to the average pLDDT of these specific residues. This method led to the identification of four main clusters and one outlier.

Cluster 1, which has the highest certainty score (pLDDT = 90.3 ± 2.3), consists of models where the majority of the SF carbonyl oxygens point inward toward the central axis, resembling the open-state SF. In contrast, cluster 2 (pLDDT = 85.2 ± 1.6) predominantly shows the carbonyl of SF residue V625 flipped outward from the central axis, along with a noticeable narrowing between the G626 carbonyls. Cluster 3 (pLDDT = 77.5 ± 2.5) is characterized by the reorientation of the G626 carbonyls and occasionally F627. In most models from cluster 2 and beyond, the S6 helix rotates to varying degrees, causing the side chains of the pore-lining, drug-binding residues Y652 and F656 to rotate and extend further into the hERG inner cavity. Both cluster 4 and the outlier cluster have low average pLDDTs (<70), making them unreliable for further analysis.

Interestingly, the inactivated state SF conformations predicted by AlphaFold coincide with proposed hERG C-type inactivation mechanisms as highlighted in other experimental and computational studies (Lau et al., 2024; Li et al., 2021). Specifically, the flipping of V625 and the constriction at G626 carbonyls in cluster 2, was previously reported in a recent study (Lau et al., 2024). Moreover, Li *et al.*'s computational work revealed an asymmetric SF conformation, where two opposing subunits exhibited similar V625 flipping and G626 narrowing characteristics, while the other two subunits displayed the G626 and F627 carbonyl reorientation characteristic of our cluster 3 (Li et al., 2021). Remarkably, AlphaFold2 was able to independently predict these conformations, despite the fact that they were not part of its training dataset, which had a cutoff year of 2021 (Jumper et al., 2021a) and did not include simulated models. Since cluster 1 SF closely resembles the open-state SF, we picked the best model from cluster 2 for further analysis and simulations, which consistently shows flipping of V625 carbonyls and pinching between G626 carbonyls across all subunits.

Open-state clusters: We combined parts of the presumed open-state cryo-EM hERG structure (PDB 5VA2) (Wang and MacKinnon, 2017), specifically the conductive selectivity filter, the activated VSDs, and the cytosolic domain, as the structural template for AlphaFold2 to test whether it would predict changes to the pore region similar to those observed in other states' predicted clusters. Post-prediction, all 100 generated models are nearly identical, converging almost uniformly into a single cluster. The highest scoring model closely mirrors the experimental open-state structure (Wang and MacKinnon, 2017), showing no major changes in the pore region.

Comparison of hERG channel states models reveals structural differences in the selectivity filter and channel pore

After further structural refinement in Rosetta (Fleishman et al., 2011; Leman et al., 2020) to resolve steric clashes, the resulting models are compared in **Figure 3**. In **Figure 3a, b**, the closed-state model displayed the most constricted channel pore, followed by the inactivated-state and then the open-state model. In the pore-lining S6

5

helix, the canonical drug-binding residue Y652 (Vandenberg et al., 2012) retains a relatively consistent position with minor variation across all channel state models. The rotation and shift of the S6 helix in the inactivated and closed states affect the position of another canonical drug-binding residue, F656 (Vandenberg et al., 2012). The adjustment caused the F656 side chain to extend more into the hERG inner cavity in both the closed and inactivated states, compared to the open state.

Shown in **Figure S1a, b**, the SFs of the open- and closed-state models display similar conformations, with carbonyl oxygens along the ion path all oriented toward the central axis as in other K^+ channel structures, e.g., KcsA and $K_V1.2$, enabling efficient knock-on K^+ conduction (Doyle et al., 1998; Long et al., 2005). In contrast, the inactivated-state model SF is distinct, marked by the lateral rotation of the V625 backbone carbonyls away from the central axis **(Figure S1c)**, thereby creating a potential barrier preventing ion crossing from the S3 to S2 binding site. Additionally, we noted a constriction between the G626 backbone carbonyls and a repositioning of the S624 sidechain hydroxyl oxygens. In the model representing the inactivated state, the carbonyl oxygens of G628 and F627 exhibit an upward shift relative to their positions in the open-state model. **Figure S1d-f** presents the SF of all three models from an extracellular perspective. In both the closed- and inactivated-state models, the F627 side chain undergoes a clockwise rotation when contrasted with its orientation in the open state. This rotational behavior aligns with findings from prior simulation study (Miranda et al., 2020) where it was noted in a metastable non-conductive state. The loop that links the upper SF to the S6 helix rotates anti-clockwise relative to its position in the open-state model, consequently narrowing the upper part of the SF.

For the VSD, we measured the distances between the backbone C_α atoms of the gating charge residues (K525, R528, R531, R534, R537, K538) on the S4 helix and the gating charge transfer center residue F463 on the S2 helix, as shown in **Figure 3c**. Although we observed an increased distance between the gating charge residues and the charge transfer center residue in the closed state, this separation was not due to a straight downward movement of the S4 helix. Instead, the closed-state model S4 exhibited a minor kink around residue R531 and lateral movement toward the channel center, impacting the S4 – S5 linker and consequently nudging the S5 helix inward, effectively narrowing the pore. The predicted closed-state model exhibits lower confidence levels for the S4 helix and S4-S5 linker residues (pLDDT ≤ 75) when compared to their counterparts in models of other states, necessitating caution in interpreting the physiological implications of this observation. Conversely, the pore region, which demonstrates closure, is characterized by a higher prediction confidence (pLDDT ≥ 75), suggesting a more robust and reliable structural representation. **Supporting Movie 1** shows an animation of state changes of the hERG channel models.

We aimed to further investigate the molecular interactions that contributed to channel inactivation through modulation of the selectivity filter conformation. In **Figure S2**, we analyzed interactions of extracellular S5-P linker (I583 – Q592) along with SF and surrounding SF residues (S620 – N633, **Figure S2a**) through heatmaps detailing hydrogen bonding, π stacking, cation-π, and salt bridge formation similarities and differences (**Table 1** shows detection criteria; distance-based contact maps (Noel et al., 2012) for all residues are shown in **Figure S3**). Distinct interaction patterns between open- and inactivated-state models were observed in these regions **(Figure S2b, c)**. In the open-state model, N633 atop the SF forms hydrogen bonds with S5-P linker G584 and Q592 from an adjacent subunit, while N629 forms hydrogen bonds with an adjacent-subunit S631. Additionally, SF G626 forms an intra-subunit hydrogen bond with S620 behind the SF. Within the S5-P linker, N588 and D591 also display hydrogen bonding. However, these stabilizing interactions in the open-state model SF region are absent in the inactivated-state model, where only intra-subunit hydrogen bonds between I583 (S5-P linker) and N633 (SF) occur, along with V630 hydrogen-bonding with the same-subunit N629 atop the SF. To corroborate our findings, mutations involving the residues discussed above have been shown to impact hERG inactivation as evidenced in numerous clinical and experimental studies (Butler et al., 2018; Clarke et al., 2006; Cordeiro et al., 2005; Dun et al., 1999; Fan et al., 1999; Ficker et al., 1998; Miranda et al., 2020; Nakajima et al., 1998; Satler et al., 1998) (see **Table 2** for more details).

There are fewer differences between the open- and closed-state models **(Figure S2b, d)**. In the open-state model, D591 from the S5-P linker forms intra-subunit hydrogen bond with N588, and G584 hydrogen-bonds with N633 at the top of the SF. These interactions are absent in the closed-state model, where H587 (instead of N588) hydrogen-bonds with D591 within the S5-P linker, and I583 (replacing G584) interacts with N633 at the SF top. Additionally,

G628 from an adjacent subunit forms a hydrogen bond with N629 atop the SF. Analyzing the differences between the inactivated- and closed-state model **(Figure S2e)**, the inactivated-state model uniquely features an intra-subunit V630-N629 hydrogen bond, whereas the closed-state model exhibits intersubunit hydrogen bonds between N633 and Q592, and between S631/G628 and N629. Furthermore, in the closed-state model, S620 forms an intra-subunit hydrogen bond with G626, stabilizing the SF conformation.

In **Figure S4**, we compared the S6 pore-lining helix orientation across various models. The closed-state model features a straight S6 helix with a minor kink. On the contrary, both the open- and inactivated-state models exhibit a pronounced kink around I655, as identified in a prior study (Thouta et al., 2014), which facilitates pore opening and distinguishes the inactivated-state from the closed-state model. Notably, a slight rotation differentiates the S6 helix in the open- and inactivated-state models, altering the conformation of drug-binding residues Y652 and to a greater extent, F656. The interaction network analysis results from **Figure S2b, c** suggest that alterations in the hydrogen bond network around the SF region, during the transition from open to inactivated state, might pull on the S6 helix and influence its orientation **(Figure S1e, f)** – a subtle yet potentially impactful change for drug binding. In agreement with our observations, a study by Helliwell *et al.* (Helliwell et al., 2018a) also suggested that a slight clockwise rotation of the S6 helix in the hERG open-state cryo-EM structure (Wang and MacKinnon, 2017) could align the S6 aromatic side chains, particularly F656, into a configuration enabling interactions with inactivation-dependent blockers that more accurately reflects experimental data (Helliwell et al., 2018b).

Molecular dynamics simulations show K$^+$ ion conduction in the open-state model but not in the inactivated state

We performed all-atom molecular dynamics (MD) simulations on two hERG channel models described above, one in the open state and the other in the predicted inactivated state, to evaluate their ion conduction capabilities. Unlike the closed-state model, both open- and inactivated-state models should allow ions and water to enter and traverse the channel pore reaching the SF region. However, only the open state-model is expected to facilitate ion conduction through its SF.

To investigate ion conduction in the selectivity filter, we considered two conditions, as shown in **Figure S5a**: one in which the SF initially contained only K$^+$ ions and another in which both ions and water were present to test previously proposed direct (or Coulombic) and water-mediated K$^+$ conduction knock-on mechanisms (Lam and de Groot, 2023; Roux, 2017) as in a previous study (Miranda et al., 2020). In the direct knock-on (ions-only) scenario, we manually positioned K$^+$ atoms in the putative K$^+$ binding sites of S0, S2, S3, and S4 within the SF. For water-mediated knock-on (the alternating ions and water molecules) scenario, K$^+$ ions were placed in the S1, S3, and S$_{cav}$ positions, while water molecules were inserted into the S0, S2, and S4 positions. These models were incorporated into phospholipid bilayers consisting of *1-palmitoyl-2-oleoylphosphatidylcholine* (POPC) molecules and hydrated by 0.30 M KCl, as depicted in **Figure S5b**. Subsequently, we conducted MD simulations for each case under three membrane voltage conditions: 0 mV, 500 mV, and 750 mV, each lasting 1 µs. This resulted in a total of six MD simulations for each model.

In all instances where a non-zero membrane voltage was applied after equilibration, we observed K$^+$ conduction for the open-state model (**Figure 4a, c** and **Figure S6a, c**), whereas such conduction was not observed for the inactivated-state model (**Figure 4b, d** and **Figure S6b, d**). For ions-only initial SF arrangement we observed that all K$^+$ ions initially located in the SF went across during 1 µs MD runs under applied 750 and 500 mV membrane voltages (**Figure 4a** and **Figure S6a**), whereas for the alternating water-ion initial SF configuration we observed conduction of SF ions as well as additional K$^+$ ions moving all the way across the channel pore (**Figure 4c** and **Figure S6c**). In both cases we saw combination of direct and water-mediated knock-on mechanisms as in our previous hERG channel MD simulations (Miranda et al., 2020; Yang et al., 2020). Control MD simulations conducted under zero voltage conditions revealed a single K$^+$ SF conduction event for the open-state model **(Figure S6g)**

when the SF was initially filled with water molecules and ions, while no conduction events were observed in the remaining cases **(Figure S6e, f, h)**.

Subsequently, we conducted an analysis of pore radius changes throughout the MD simulations (see full results in **Figure S7**). In under zero voltage conditions, we observed consistent and distinct pore radius profiles across all simulations within their respective models (left panel in **Figure S8a**). Specifically, MD simulations featuring the inactivated-state model consistently displayed a narrower pore radius when compared to simulations involving the open-state model. However, when subjected to high voltage conditions, the open-state model exhibited a shift towards an inactivated-like state, leading to a reduction in the pore width (right panel in **Figure S8a**), which is consistent with an increased hERG channel inactivation propensity at more depolarized voltages (Vandenberg et al., 2012). Although we did not observe the outward flipping of the V625 backbone carbonyl oxygens in the SF during the 1 μs simulations of the open-state model, we did observe the flipping of the F627 backbone carbonyl oxygens as shown in **Figure S8b**. Interestingly, this SF conformation with flipped F627 but not V625 is also observed in cluster 3 of the AlphaFold-predicted models shown in **Figure 2**. In the inactivated-state model MD simulations, increasing membrane voltage resulted in an increased probability of flipping of the V625 backbone carbonyl oxygens into ion conducting conformation. Notably, a single outward oriented carbonyl oxygen still prevented K^+ conduction through the SF.

Comparison with previously reported K^+ channel C-type inactivation mechanisms

Cuello *et al.* in their study of KcsA channel identified a similar constriction at G77 within the SF and a corresponding reorientation of the V76 carbonyl, resulting in a dilation in the SF at this location and corresponding loss of the S2 and S3 ion binding sites (Cuello et al., 2010). They suggested this backbone rearrangement as a fundamental molecular mechanism underlying C-type inactivation in K^+ channels (Cuello et al., 2010). In other studies on Shaker and $K_V1.3$ channels, dilation in the upper SF that disrupts the S1 and S2 K^+ binding sites has been proposed to be a potential C-type inactivation mechanism (Chandy et al., 2023; Selvakumar et al., 2022; Tan et al., 2022; Tyagi et al., 2022). Similar dilations in the SF are also predicted by AlphaFold2, particularly within cluster 3 of the predicted inactivated state hERG channel clusters shown in **Figure 2a**. Although these models were not simulated under our study, such dilated conformations of the SF also emerged during our MD simulations of the open-state model under applied voltage.

We further analyzed predicted inactivated-state conformations by plotting the cross-subunit distances between the carbonyl oxygen atoms of SF residues at 750 mV and 500 mV applied voltages, as shown in **Figure S9**. The dilation observed in the hERG channel, which also occurs in the upper SF, differs from that in the aforementioned K^+ channels. In Shaker-family channels, the most considerable widening occurs at the SF tyrosine residue (Y445 in Shaker/Y377 in $K_V1.2$) immediately below the topmost SF residue (G446 in Shaker/G378 in $K_V1.2$) (Tan et al., 2022; Wu et al., 2023). Conversely, in the hERG channel, the topmost SF residue (G628) exhibits the most significant widening, followed by the residue immediately below it (F627). Our MD simulations of the hERG channel reveal that its dilation process involves two sequential steps: SF near residues F627 dilates first, followed by SF near topmost G628 residues. The latter step occurs faster at higher voltages (750 mV) compared to lower voltages (500 mV). We present these steps in **Figure S10**. Notably, despite the dilation of the hERG SF, ion conduction is still observed across all replicas, in contrast to the Shaker channel (Chandy et al., 2023; Selvakumar et al., 2022; Tan et al., 2022; Tyagi et al., 2022).

Computational drug docking reveals state-specific differences in drug binding

We utilized Rosetta GALigandDock software (Park et al., 2021) to dock 19 drugs from different classes, considering their multiple protonation states, into our hERG state-specific channel models. This process aimed to evaluate and corroborate state-dependent binding interactions with experimental studies, specifically in terms of relative binding affinities. **Figure S11** presents these findings in the form of Rosetta GALigandDock (Park et al., 2021) binding energies (lower values mean more favorable binding). Consistent with published studies, most drugs showed stronger binding to the inactivated-state hERG channel model, including astemizole, terfenadine, cisapride, d/l-sotalol, dofetilide (Perrin et al., 2008), and E-4031 (Numaguchi et al., 2000; Wang et al., 1997). Drugs like moxifloxacin (Alexandrou et al., 2006), quinidine (Perrin et al., 2008), and perhexiline (Perrin et al., 2008) did not

8

show strong preference for the inactivated-state model, aligning with findings from hERG experimental studies using inactivation-deficient mutants (Perrin et al., 2008) or "step-ramp" voltage protocol (Alexandrou et al., 2006).

In our GALigandDock docking results, most drugs exhibited increased binding affinity to the closed-state hERG model compared to the open-state hERG model. Drugs are unable to bind to the closed state from the intracellular space because the pore is closed. However, they can become trapped if they are already bound when the channel transitions from open to closed state, as shown in experiments for dofetilide (Windley et al., 2017), cisapride (Windley et al., 2017), terfenadine (Windisch et al., 2011; Windley et al., 2017), E-4031 (Windisch et al., 2011), and nifekalant (Kamiya et al., 2006).

To model drug trapping, we placed the drug in a pocket beneath the selectivity filter in the closed pore configuration before docking. However, this method does not consider how the conformational shift from the open to the closed state might influence drug binding. Under physiological conditions, the pore gating motion from open to closed might expel drugs from the pore instead of pushing them deeper. This limitation might account for some inconsistencies noted in our docking study, particularly regarding the apparent trapping of drugs such as amiodarone and haloperidol, which is at odds with experimental results (Stork et al., 2007). However, these preliminary results could pave the way for more thorough investigations, employing advanced computational techniques to delve deeper into the dynamics of drug trapping (Branduardi and Faraldo-Gómez, 2013; Miao et al., 2020).

As an example, **Figure 5** focuses closely on the binding of astemizole, dofetilide, and quinidine in their cationic forms (the predominant species at the physiological pH 7.4) to different hERG channel models. Experimental evidence (Perrin et al., 2008) suggests that dofetilide and astemizole bind more potently to the inactivated state, while quinidine does not exhibit this preference.

Astemizole: In the open-state model, astemizole engages in π stacking with the Y652 aromatic side chain via its benzimidazole group and forms hydrophobic contacts with adjacent residues (A653 and F656) and Y652 from another subunit. Its binding occurs just below S6 helix residue Y652, not deeply within the pore, resulting in a binding pocket that remains partially open to external solvent. In contrast, in the inactivated-state model, astemizole demonstrates an increase in interactions and becomes fully enclosed within the binding site deeper into the pore, engaging in hydrophobic interactions with S6 residues S649, Y652, F656, and S5 residue F557. The astemizole methoxyphenyl group engages in the π stacking with hERG Y652 and F656 side chains from adjacent subunits. At the other end, the aromatic ring of Y652 hydroxyphenyl side chain also engages in π stacking, while its oxygen atom acts as a weak hydrogen bond acceptor (i.e., donor angle of ≤ 45° and bonding distance of ≤ 3.8 Å) to astemizole secondary amine group. Furthermore, the SF residue S624 side chain participates as a hydrogen bond acceptor with the cationic ammonium group of astemizole piperidine ring. The binding pattern in the closed-state model is similar to that in the inactivated-state model, but it includes additional hydrophobic interaction with G648 and I655.

In 2021, a study by Asai *et al.* solved the cryo-EM hERG structure in complex with astemizole (Asai et al., 2021). Although the structure deposited to the PDB (7CN1) (Asai et al., 2021) did not include ligand coordinates, a possible astemizole binding pose was suggested based on residual EM density. The density map showed a π-π interaction of astemizole with Y652 and a hydrogen bond with S624 (Asai et al., 2021). In addition, electrophysiology study by Saxena *et al.* has identified F557 and Y652 as crucial for astemizole binding, as determined through mutagenesis (Saxena et al., 2016).

Dofetilide: In the open-state hERG model, dofetilide interacts with multiple residues of the pore lining S6 helices. For instance, it forms hydrogen bonds with two S660 residues from opposite subunits and two A653 residues from adjacent subunits. Additionally, there are hydrophobic interactions with Y652 and G657. When bound to the inactivated-state hERG model, dofetilide settles deeper into the pore, extending horizontally above the Y652 residue, where it forms π stacking and cation-π interactions, as well as hydrogen bonds with the Y652 residues of all subunits. The backbone carbonyl oxygen of residue S649 also engages in hydrogen bonding with the nitrogen in the sulfonamide group of dofetilide. There are also hydrophobic contacts with hERG S6 residues S649, F656, and I655 as well as residue F557 on the S5 helix. The closed-state model pore provides a substantially narrower space, leading dofetilide to bind vertically along the pore axis, forming hydrophobic contacts with S624, S649, Y652,

F656, and S660. Here, the oxygens and nitrogen of its sulfonamide group create a series of hydrogen bonds with hERG residues T623 and Y652. The central cationic tertiary ammonium group of the ligand forms cation-π interactions with two F656 residues from adjacent subunits. Lastly, the oxygens in the remaining sulfonamide group are involved in hydrogen bonding with the S660 residues from 3 subunits. In the inactivated-state and closed-state models, the binding pocket is completely enclosed, unlike the open-state model.

In line with our results, mutations of A653 affected hERG channel blocking by dofetilide (Stepanovic et al., 2009). Additionally, electrophysiology study by Saxena *et al.* revealed that mutants Y652A and F557A altered dofetilide-induced hERG inhibition (Lees-Miller et al., 2000; Saxena et al., 2016). Another experimental mutagenesis study by Kamiya *et al.* have highlighted possible dofetilide interactions with hERG S6 residues G648, Y652, F656, and V659 as well as its pore helix residues T623, S624, and V625 (Kamiya et al., 2006) in general agreement with our study.

Quinidine: Unlike the previous two drugs, quinidine does not exhibit significant state-specific binding based on our docking predictions **(Figure S11)**. In the open state hERG model, its small size allows for complete enclosure within the binding pocket, where it forms distorted hydrogen bond with residue Y652, hydrophobic contacts with another Y652 from an adjacent chain, as well as other S6 residues A653 and S660. In the inactivated-state model, quinidine binds lower in the pore, resulting in a binding pocket partially open to solvent. Here, its quinoline rings engage in π-stacking interactions with the F656 side chain above and hydrophobic contacts with another F656 from the opposite subunit. The quinidine hydroxyl oxygen forms a weak hydrogen bond with residue S660. In the closed-state model, quinidine becomes trapped deeper in the pore and is fully enclosed. Its quinoline rings π stack with multiple F656 side chains below and the Y652 side chain above drug binding position. The quinidine hydroxyl oxygen now establishes a weak hydrogen bond with Y652, with additional hydrophobic contacts observed with other Y652 and F656 side chains and the T623 backbone. Corroborating our results, Sănchez-Chapula *et al.* previously found that mutating key aromatic residues (Y652, F656) in the S6 segment reduced the efficacy of quinidine by more than 100-fold (Sănchez-Chapula et al., 2003).

Validation of state-dependent drug block with experimental data using hERG Markov model

There are several complications that make it difficult to directly compare experimental binding affinities with predicted affinities from simulations. During electrophysiological recordings of hERG inhibition by various drugs, hERG has been shown to adopt various functional states, presumably corresponding to different protein conformation states. These states can be bound by drugs with varying affinities, with drug ionization state also being a contributing factor. Additionally, the variability in experimental protocols affects the measured affinities (Gomis-Tena et al., 2020). In general, electrophysiological measurements report the IC_{50}, the drug concentration required for 50% inhibition of current. However, the IC_{50} value is not directly comparable to computed affinities from drug docking.

To address these challenges, we developed a novel computational approach that combines modeling and simulation to predict hERG channel conformational state probabilities (open, closed, inactivated) over time. First, we collected a comprehensive set of experimental data and employed a hERG functional model with five functional states, which was extensively validated in our earlier study (Romero et al., 2015). For each drug, we ran *in silico* electrophysiological experiments under the same conditions as the experimental studies, allowing us to calculate the relative probabilities of the various hERG channel states specific to the drug and protocol. These state probabilities were then used to refine the computed binding affinities from docking simulations. We adjusted the affinities for both neutral and charged forms of each drug according to their prevalence in each conformational state. This method allowed us to scale the binding predictions based on the likelihood of each channel state occurring during the experimental protocols. Finally, we compared the simulated binding affinities with experimental hERG binding potencies **(Table 3)**, offering a new validation technique that enhances the accuracy of our predictions and helps reconcile the differences between experimental IC_{50} measurements and computed affinities.

We compared the experimental drug binding potencies with the simulated binding affinities, starting with the traditional approach of using only open-state drug binding simulations **(Figure 6a**, commonly used in ion channel pharmacology due to the absence of multi-state models) and then expanding to simulations that account for drug

10

binding to different states **(Figure 6b)**. The comparison revealed that while the conventional open-state drug binding model showed a moderate correlation with experimental drug potencies (R^2 = 0.45, Pearson's r = 0.67, p-value = 0.00046), including multi-state binding improved how well the model explained the experimental data by 35.6% (R^2 increased to 0.61) and strengthened the correlation (Pearson's r increased to 0.78, p-value = 0.00001).

This improvement highlights the importance of including multiple conformational states in drug docking simulations, offering a more complete view of how the drug interacts with the ion channel. It also further supports potential physiological relevance of our predicted inactivated and closed state hERG channel models. Notably, this stronger correlation was achieved without considering how drugs may influence ion channel gating dynamics — an aspect that could further refine our predictions and will be addressed in future studies. Despite these limitations, the results suggest that multi-state drug binding simulations may provide a more reliable approach than conventional single-state ion channel models, showing promise for more accurate drug potency predictions in ion channel pharmacology.

Discussion

In this study, we introduced a methodology to extend AlphaFold2's predictive capabilities by guiding it to sample multiple protein conformations reminiscent of different ion channel states, using the hERG potassium channel as a proof of concept. While other studies have focused on generating diverse conformations, we aimed to take this further by validating the physiological relevance of these predicted states through computational simulations and experimental data. By incorporating multiple structural templates and refined input parameters, we directed AlphaFold2 to predict distinct functional states, including the closed and inactivated forms of hERG. This validation is particularly important, as understanding the full conformational spectrum of a protein can provide valuable insights for pharmacological development, especially for an anti-target like hERG, which exhibits state-specific drug interactions (Li and Ramos, 2017; Perrin et al., 2008; Sanguinetti and Tristani-Firouzi, 2006; Vandenberg et al., 2012; Yang et al., 2020). Such knowledge can aid in designing safer drugs that avoid undesirable interactions, such as drug-induced cardiotoxicity, by selectively targeting or avoiding particular hERG channel states. This proof of concept illustrates the potential of our methodology for hERG and offers a framework that could be extended to other membrane proteins, contributing to advancements in *in silico* drug safety assessments and development.

The first strategy involved using AlphaFold2 as a generative tool, where we provided structural fragments indicative of a specific state of the channel as templates and instructed AlphaFold2 to reconstruct the remaining structure from these fragments. This approach was particularly effective in modeling the hERG channel in its closed state with a non-conductive constricted pore. The second strategy focused on using AlphaFold2 to investigate a wide range of potential conformational states, especially in scenarios where there is limited knowledge. Remarkably, AlphaFold2 managed to generate conformations that had been previously documented in the literature (Lau et al., 2024; Li et al., 2021) but not included in the training dataset, showcasing its broad predictive capacity. We further validated the physiological significance of these states using computer simulations and comparing them to experimental results as discussed below. This methodology has provided new insights into the structural and functional behavior of the hERG channel, including state-specific drug interaction mechanisms.

The predicted models of the closed, open, and inactivated states of the hERG channel, have revealed detailed structural aspects that were previously elusive, particularly in the pore region where drug binding occurs. The closed-state hERG channel model demonstrates constricted pore and deactivated voltage-sensing domains, suggesting a structural basis for channel deactivation. Conversely, the open state hERG channel model indicates a pore conformation that allows ion conduction and aligns with the physiological role of the channel in cardiac repolarization. The inactivated-state hERG channel model suggests a non-conductive selectivity filter conformation with notable changes to the pore region that underpin new insights into state-specific drug-induced channel blockade. The structural models similar to ones predicted in our study have not been published in any publicly available databases and were not used for training AlphaFold2, to our knowledge. Our approach thus underscores the substantial yet untapped potential of AlphaFold2 to predict *de novo* channel conformations with physiological relevance.

One of the most compelling predictions here is that AlphaFold2 predicted models that directly corresponded to the previously reported "inactivated state" conformations from prior experimental and simulation studies. These structures were identifiable in discrete protein clusters **(Figure 2a)** with high prediction confidence metrics and likely together constitute components of the hERG inactivation mechanism. In this way, AlphaFold2 provided a strong method to reconcile apparently disparate previous experimental and computational data.

Predicted by AlphaFold2 and validated in our study, the non-conductive SF conformation is characterized by the flipping of SF V625 carbonyl oxygens away from the central axis and minor constriction at the level of G626. Echoing our observations, Lau et al. suggested that such flipping may constitute a C-type inactivation mechanism for the hERG channel (Lau et al., 2024). Their study involved altering the external K^+ concentration to predispose the channel towards a non-conductive, presumed inactivated state (Lau et al., 2024). Li et al. made a similar observation in their computational study, demonstrating the constriction between G626 carbonyls which occurs asymmetrically in only two opposing subunits and not in the others to be a potential C-type inactivation mechanism (Li et al., 2021). Indeed, this constriction was accompanied by the flipping of V625 carbonyls in the same subunits where the constriction was observed (Li et al., 2021). Although these studies have proposed potential molecular mechanisms for hERG C-type inactivation (Lau et al., 2024; Li et al., 2021), they have primarily concentrated on conformational shifts leading to a non-conductive selectivity filter. Our study takes a step further and sheds light on how these alterations extend to the pore region and subsequently impact drug binding as seen in experiments, which is an outstanding issue in safety pharmacology and drug development as hERG channel is a notorious drug anti-target (Perrin et al., 2008; Yang et al., 2020).

For other K^+ channels, dilation in the SF has been proposed to be potential C-type inactivation mechanisms (Chandy et al., 2023; Cuello et al., 2010; Selvakumar et al., 2022; Tan et al., 2022; Tyagi et al., 2022). While inactivation processes across various K^+ channels may share some similarities, the associated conformational changes can adopt distinct differences due to small variations in the SF sequences, which could explain the observed variability in inactivation rates among hERG and other ion channels (Vandenberg et al., 2012). As an example, a study on Shaker-family channels suggested that a two-step widening process in the upper SF could be a mechanism for C-type inactivation (Wu et al., 2023). The SF of Shaker-family channel has the sequence "TVGYGD". The first step involves a partial twist of the P-loop backbone, particularly involving the upmost SF residue D30' (D379 in $K_V1.2$), which originally stabilizes itself by interacting with W17' (W336 in $K_V1.2$). The second step is the reorientation of the upper-middle SF residue Y28' (Y377 in $K_V1.2$) upward, which normally participates in hydrogen bonds with nearby pore-helix residues, to fill some of the original volume occupied by D30'.

In contrast, the hERG SF is characterized by the sequence "SVGFGN". In the upper SF of the hERG channel, phenylalanine (F) replaces the tyrosine (Y) found in many K^+ channels including Shaker and $K_V1.2$. Phenylalanine has a non-polar benzyl side chain, whereas tyrosine has a polar hydroxyl group attached to its benzene ring. The hydroxyl group in tyrosine can form additional hydrogen bonds, which may stabilize different SF conformations in other K^+ channels compared to hERG. Similarly, at the outermost end of the selectivity filter of hERG, asparagine (N) replaces the aspartate (D) found in many other K^+ channels. Asparagine is uncharged, while aspartate introduces a negative charge through its carboxylate group, which could explain the differences in ion coordination and gating dynamics. These structural differences may explain why hERG channel adopts a similar but distinct SF rearrangement compared to other K^+ channels (such as Shaker and $K_V1.2$) and can have a slightly different structural mechanism of the C-type inactivation.

Molecular dynamics simulations were crucial in confirming conformational state functional properties. The observed differences in ion conduction between the predicted open and inactivated hERG channel states illustrate the impact of structural changes on ion channel activity. In addition, the drug docking analysis matched expectations, with significant preference for the inactivated-state model across a variety of hERG blockers. In most cases, the increased drug binding affinity to the inactivated state hERG model can be attributed to the protrusion of residue F656 aromatic side chain into hERG central cavity (**Figure 3a**). This protrusion has the potential to strengthen drug binding through providing extra π stacking or hydrophobic interactions. Additionally, the side chains of F656 may act as a barrier, blocking drugs that are bound deeper within the pore from escaping even when they do not have direct interactions with the drugs. Similar observations were made for the closed-state model, where the pore closure also positions the F656 side chains into the central cavity. In addition, the slanted orientation of the Y652

12

aromatic rings and repositioning of the S624 sidechain hydroxyl oxygens in the inactivated-state model enabled the formation of a binding pocket between S624 and Y652 (**Figure 3b**, at Z = 21 Å), enabling drugs to reach deeper into the pore.

Furthermore, we carried out molecular docking of multiple drugs to test their state-dependent binding preferences and relative affinities. An additional novelty of our study was the development of a new computational modeling and simulation approach that allowed us to use the predicted affinities of drug binding from docking simulations and compare them directly to measured hERG channel inhibition potencies from electrophysiology experiments. We employed a simulated hERG functional model comprising of five functional states that we have extensively validated in our earlier studies (Romero et al., 2015) and performed *in silico* electrophysiological experiments under the same conditions as reported in the experimental papers. In doing so, we could compute the relative hERG channel state probabilities during the experimental protocol. The channel state probabilities were then used to scale the computed affinities in each state from the docking simulations, allowing comparison of the overall computed relative affinity with experimentally reported relative potencies. Such an analysis created an opportunity for an "apples-to-apples" comparison between structurally derived affinity predictions and abundant functional measurements that have been conducted for half a century. This novel linkage can be readily expanded to other protein targets and any variety of drugs. The intersection of structural modeling, molecular docking and functional simulations, and supporting experimental data offers a comprehensive approach to understanding protein structures and their links to biological functions.

Despite the promising results, our study is not without limitations. While AlphaFold has demonstrated remarkable accuracy in numerous instances (AlQuraishi, 2019; Jumper et al., 2021b; Varadi and Velankar, 2023), it is important to note that the predicted models may not always be reliably accurate to assess drug binding (Karelina et al., 2023). Moreover, hERG channel inactivation and closure might encompass a range of states as was shown for other ion channels (Catterall et al., 2020; Goldschen-Ohm et al., 2013; Hite and MacKinnon, 2017; Li et al., 2024; Yao et al., 2023), and the conformations we have identified could potentially represent just a few possibilities within this broad spectrum. Recently, AlphaFold3 was released, incorporating a diffusion model that enables the prediction of proteins in complex with other proteins, small molecules, nucleic acids, and ions (Abramson et al., 2024). Although AlphaFold3 demonstrated high accuracy in various predictive tasks and is expected be widely adopted, the source code is not publicly available. Consequently, the approaches employed in this study with AlphaFold2 cannot yet be applied to AlphaFold3. The results from GALigandDock drug docking, while providing valuable insights, should be regarded as provisional at this juncture (Maly et al., 2022). Correlating simulated drug binding affinities with experimental results is challenging because multiple studies have shown that drug binding potency is highly dependent on the measurement technique used, resulting in different IC_{50} values being reported for the same channel – drug pairing (Alexandrou et al., 2006; Asai et al., 2021; Cameron et al., 2021; Chiu et al., 2004; Ficker et al., 1998; Hansen et al., 2006; Johnson and Trudeau, 2023; Kushida et al., 2002; Orvos et al., 2019; Paul et al., 2002; Perrin et al., 2008; Rampe et al., 1997; Suessbrich et al., 1997; Tanaka et al., 2014; Walker et al., 1999; Zhang et al., 1999; Zhou et al., 1998) as was explored in detail in our recent study (Gomis-Tena et al., 2020). Additionally, knowing the binding free energies of a drug is not the complete story; binding rates such as k_{on} (association rate) and k_{off} (dissociation rate) are also crucial for a quantitative evaluation of drug binding to the channel. The results herein primarily serve as a basis for further detailed investigation using methods like molecular dynamics simulations linked to multiscale functional modeling, as demonstrated in our previous studies (DeMarco et al., 2021; Yang et al., 2020).

In conclusion, this study not only advances our knowledge of the hERG channel structural dynamics and state-dependent drug binding but also sets a precedent for using AlphaFold2 or similar computational methods, such as RoseTTAFold (Baek et al., 2021) and ESMFold (Lin et al., 2023), to study other ion channels and membrane proteins. The insights gained from this study are expected to have a lasting impact on the fields of ion channel physiology and pharmacology, including cardiac drug safety, providing a foundation for future research aimed at developing safer and more effective therapeutic agents.

Materials and Methods

hERG channel model generation and refinement with AlphaFold2 and Rosetta

AlphaFold2 employs a deep learning architecture that integrates several innovative components including, residue pair representation comprising an architecture module that represents each possible pair of amino acid residues in the sequence. This pairwise representation captures the interactions between residues that determine the protein folding. AlphaFold2 also applies an attention mechanism, which constitutes a transformer-based model (similar to the architecture used in natural language processing) to weigh the influence of different parts of the input data differently (Jumper et al., 2021a). In AlphaFold2, the effect is to emphasize interactions between certain amino acid residues more than others based on how they might impact folding. There is also a so called Evoformer block within the learning model that specifically processes the evolutionary data from multiple sequence alignments, enabling the model to effectively incorporate evolutionary information (Jumper et al., 2021a). After processing through the Evoformer, intermediate representations are used to predict the distances and angles between residues as part of an iterative feedback process. One of the most critical pieces of the AlphaFold2 architecture is the recycling layers that promote an iterative refinement of predictions. The output from each iteration of the model feeds into the next one as input. This process, known as "recycling", helps refine the accuracy of the predicted structure with each pass.

Due to the time-intensive process of creating multiple sequence alignments (MSA) for AlphaFold2, the ColabFold (Mirdita et al., 2022) software was made to streamline protein structure prediction by combining MMseqs2 (Mirdita et al., 2019) sequence search toolkit with AlphaFold2, enhancing runtime efficiency while preserving high prediction accuracy. First, we provided this hybrid structure as a template for ColabFold. ColabFold utilized only a portion of the MSA in the modeling process to reduce memory usage. We adjusted the limit to 256 cluster centers and 512 additional sequences (*max_msa* = "256:512"), a reduction from the standard values of 512 and 1024, respectively. Altering the random seed can lead to variance in cluster centers and, consequently, in structure predictions. Therefore, we set AlphaFold2 to cycle through 20 random seeds (each seed was used to produce 5 models) to foster diversity in the predicted conformational states (*num_seeds* = 20), resulting in 100 total models per run. An exception to this approach was the initial phase of inactivated-state hERG model creation, where a single seed number was used to generate 5 models. Additionally, we enabled the model stochastic component (*use_dropout* = True) during the inference pipeline to sample from an ensemble of models for the more ambiguous segments of the structure prediction. The number of iteration cycles was set to 20, with an early stopping tolerance of 0.5 based on per-residue confidence metric pLDDT deviation from the previous cycle. Structures were converted from the PDB file format to CIF prior to being used as templates in ColabFold. Previous studies indicated that these settings may permit the sampling of alternative protein conformations (Brown et al., 2024; del Alamo et al., 2022; Mirdita et al., 2022; Sala et al., 2023). The N-terminal PAS domain (residues M1 – R397) was not included in the modeling due to graphics card memory limitation making the resultant model (W398 – R863) resemble hERG 1b isoform (Phartiyal et al., 2007).

Structural data for the hERG channel in its open state (PDB 5VA2) (Wang and MacKinnon, 2017) were sourced from the Protein Data Bank (PDB) (Berman et al., 2000), and missing segments of the loops were modeled using Rosetta (Leman et al., 2020) software suite LoopRemodel (Huang et al., 2011). This reconstructed open-state model served as a basis for molecular dynamics and drug docking simulations. However, we also wanted to test the potential for AlphaFold2 to emulate the open state model. To do so, specific regions of the putative open state hERG model (PDB 5VA2) (Wang and MacKinnon, 2017) — namely the VSD (W398 – V549), the SF with adjacent pore helix (I607 – T634), a part of S6 helix and the cytosolic domain (S660 – R863) — were provided to ColabFold as structural templates. Then, 100 diverse models were generated for further analysis.

Post-prediction, the resulting 100 models for each structural state were categorized into clusters based on all-atom RMSD between those models. Closed-state models were clustered with a threshold of 0.75 Å across the entire channel, whereas inactivated and open states (non-empirical, AlphaFold-predicted) models focused on the SF (residues S624 – G628), with a more stringent threshold of 0.35 Å. We ranked the models in the cluster by their average per-residue confidence metric (predicted local distance difference test, or pLDDT), which assesses the likelihood that the predicted structure aligns with an experimentally determined structure (Jumper et al., 2021a).

14

pLDDT above 90 are considered to be highly reliable and those between 70 and 90 as reliable with generally good protein backbone structure prediction (Jumper et al., 2021a). Lower scores indicate regions of lower confidence and may be unstructured. Cluster 1 is defined in this study to be the cluster with highest average pLDDT among all the clusters.

Afterward, we refined the preliminary atomistic structural models putatively representing each functional state of the hERG channel (open, inactivated and closed) using Rosetta FastRelax protocol (Fleishman et al., 2011; Leman et al., 2020) with an implicit membrane to optimize each residue conformation and resolve any steric clashes. The protocol was set to repeat 15 times and included an implicit POPC membrane environment. For each final model, 10 separate relaxation runs were executed, and the highest-scoring model from these runs was selected for further simulations and analyses.

Atomistic MD simulations of hERG channel conduction

The CHARMM-GUI web server (Jo et al., 2008) was employed to embed hERG channel structural models within tetragonal patches of phospholipid bilayers, each comprising approximately 230 to 240 POPC lipid molecules. The resulting assemblies were immersed in a 0.3 M KCl aqueous solution, culminating in molecular systems with an approximate total of 138,000 to 144,000 atoms. Residue protonation states were determined assuming a neutral pH=7.4 environment, and each channel subunit was terminated with standard charged N- and C-termini.

MD simulations were conducted using the Amber22 (Case et al., 2005) software suite. The simulations utilized standard all-atom Chemistry at Harvard Macromolecular Mechanics (CHARMM) force fields such as CHARMM36m (Huang et al., 2017) for proteins, C36 (Klauda et al., 2010) for lipids, and standard ion parameters (Beglov and Roux, 1994), in conjunction with the TIP3P water model (Jorgensen et al., 1983). The systems were maintained at 310.15 K and 1 atm pressure in the isobaric-isothermal (*NPT*) ensemble, facilitated by Langevin thermostat and the Berendsen barostat. Non-bonded interactions were calculated with a cutoff of 12 Å. Long-range electrostatic forces were computed using the Particle Mesh Ewald (PME) method (Darden et al., 1993), and van der Waals interactions were not subjected to long-range correction as per recommendations for the C36 lipid force field (Klauda et al., 2010). All hydrogen-connected covalent bonds were constrained using the SHAKE algorithm to enable a 2-fs MD simulation time step (Ryckaert et al., 1977).

Equilibration began with harmonic restraints imposed on all protein atoms and lipid tail dihedral angles, initially set at 20 kcal/mol/Å² and reduced to 2.5 kcal/mol/Å² over 6 ns. A subsequent 90 ns equilibration phase further decreased the restraints to 0.1 kcal/mol/Å², initially encompassing all atoms in the protein and eventually focusing solely on the backbone atoms of pore-domain residues (G546 to F720). In selected MD simulations, an electric field was applied along the *Z* direction to mimic membrane voltage (Gumbart et al., 2012), increasing linearly over the final 10 ns of equilibration to reach either 500 or 750 mV. This setup prefaced a production phase lasting 910 ns, totaling 1 µs of total simulation time per each case.

Docking of small-molecule drugs to hERG channel models

Ligand structures (i.e., pharmaceutical compounds) were retrieved from the PubChem (Kim et al., 2016) and ZINC (Tingle et al., 2023) databases. In this study, we considered the protonation states of the top two most dominant species at the physiological pH of 7.4, computed using the Henderson–Hasselbalch equation. After these initial modifications, each ligand partial atomic charges, as well as atom and bond types, were refined using AM1-BCC correction via the Antechamber module in AmberTools22 (Case et al., 2023, 2005).

Each ligand was individually positioned within the pore of the hERG channel, specifically between the key drug-binding residues, Y652 and F656, located on the pore-lining S6 helices. This manual placement was a preparatory step for the docking process. Docking was executed using the GALigandDock (Park et al., 2021) Rosetta mover, a component of the Rosetta software suite (Leman et al., 2020). The *DockFlex* mode was utilized for this purpose with a spatial padding of 5 Å. For every individual hERG channel – ligand pair, a total of 20 parallel runs were conducted. Each run generated 1,250 unique docking poses, cumulatively providing a substantial collection of 25,000 poses for each ligand – hERG channel complex. This extensive array of poses was intended to ensure a

15

comprehensive exploration of potential ligand binding configurations and orientations within the hERG channel pore.

Utilizing in-house Python scripts, we selected the top 50 docking poses for each ligand based on the lowest free energy of binding as calculated by GALigandDock. These selected poses were then clustered based on ligand all-atom RMSDs, factoring in the symmetry of the hERG channel to ensure accurate grouping. The clustering was executed with an RMSD threshold of 2.5 Å, and only clusters containing a minimum of 8 poses were deemed significant; those with fewer were classified as outliers. Within the cluster with the most favorable average binding free energy, we selected the top scoring pose as the representative pose for further analysis. This pose was then subjected to a detailed analysis of protein-ligand interactions utilizing the Grapheme Toolkit from the OpenEye software suite (www.eyesopen.com). The criteria for detecting interactions are outlined in the OEChem Toolkit manual (https://docs.eyesopen.com/toolkits/python/oechemtk/OEBioClasses/OEPerceiveInteractionOptions.html), with two modifications to minimize clutter: the *MaxContactFraction* is set to 1 (default: 1.2), and the *MaxCationPiAngle* is adjusted to 30° (default: 40°). The interaction patterns and binding sites were subsequently rendered as a two-dimensional image for comprehensive visual interpretation. Additionally, for a more detailed understanding of the spatial arrangement, three-dimensional visualization of the protein-ligand complexes was conducted using the ChimeraX (Pettersen et al., 2021) software.

Calculation of state probabilities using a five-state hERG Markov model

Over the time course of experimental recordings of hERG inhibition by various drugs, the channel can be in different functional states, each bound by drugs with different ionization states, making it difficult to compare experimental and simulated binding affinities. Moreover, different studies utilize different electrophysiological protocols to measure state-dependent ligand binding, further complicating comparisons. To address this complication, we used a five-state hERG Markov model to predict the probabilities of the channel in each state (open, closed, inactivated) during a given experimental protocol (Romero et al., 2015). Transition rate constants are provided in **Table 4**. The protocols that were used in the model to calculate each state probabilities (closed states: C3 + C2 + C1, inactivated state: I, and open state: O) are shown in **Table 5**. To simulate the inhibitory effects of drug on the hERG channel current, I_{Kr}, we decreased the peak conductance, G_{Kr} in a concentration dependent fashion using a concentration response relationship with a Hill coefficient of 1 ($n = 1$) as follows:

$$G_{Kr} = G_{Kr,max} \left(\frac{1}{1 + ([Drug]/IC_{50})^n} \right)$$

where $G_{Kr,max}$ is the nominal conductance value obtained from each ventricular myocyte model, [Drug] is a molar drug concentration, and the IC_{50} is the concentration of drug that produces a 50% inhibition of the targeted transmembrane current, i.e. I_{Kr} in this case (see **Table 5**).

To obtain the simulated binding affinity of a drug, $\Delta G_{bind, sim}$, we multiplied the binding affinity for each state by the probability of the channel being in that state and combined these values for both neutral and cationic forms of the drug, as represented by the following equation:

$$\Delta G_{bind, sim} = P_{drug, neutral} (\Delta G_{bind, O, neutral} \times P_{hERG, O} + \Delta G_{bind, I, neutral} \times P_{hERG, I} + \Delta G_{bind, C, neutral} \times P_{hERG, C})$$
$$+ P_{drug, cationic} (\Delta G_{bind, O, cationic} \times P_{hERG, O} + \Delta G_{bind, I, cationic} \times P_{hERG, I} + \Delta G_{bind, C, cationic} \times P_{hERG, C})$$

Here, $\Delta G_{bind, O}$, $\Delta G_{bind, I}$, $\Delta G_{bind, C}$ represents simulated binding affinities for the open, inactivated, and closed state, respectively, to either the neutral or the cationic form of the drug. $P_{hERG, O}$, $P_{hERG, I}$, $P_{hERG, C}$ represent the fraction of channels that are in the open, inactivated, and closed state, at the time when the tail current was observed in electrophysiological recordings to calculate drug fractional block, determined for the specific voltage protocol employed. $P_{drug, neutral}$ and $P_{drug, cationic}$ represent the fraction of neutral and cationic species of each drug at physiological pH 7.4 as calculated using the Henderson-Hasselbalch equation using drug pK_a values from Chemaxon. The zwitterionic species of moxifloxacin instead of cationic was included. These data are recorded in **Table 3**. Experimental IC_{50} values (in units of M) were converted to equivalent binding free energies using the equation $\Delta G_{bind, exp} = -RT\ln(1/IC_{50})$ where $R = 0.0019872036$ kcal K^{-1} mol^{-1} is the gas constant and T is the experimental temperature in K.

16

Molecular graphics and interaction analysis

Molecular graphics visualization was performed using ChimeraX (Pettersen et al., 2021). MD trajectory and simulation images were visualized using VMD (Humphrey et al., 1996). Interaction network analysis was performed using the Protein-Ligand Interaction Profiler (PLIP) (Salentin et al., 2015) with criteria outlined in **Table 1**.

Data availability

All final study data are included in the article and/or SI Appendix with key molecular modeling, docking as well as molecular dynamics simulation and analysis data files and scripts available to download from Dryad digital repository at https://doi.org/10.5061/dryad.18931zd5x. *(Note for the editor and reviewers: the link will be active after the manuscript acceptance for publication).*

Ethics declarations

Competing interests: The authors declare no competing interests.

References

Abramson J, Adler J, Dunger J, Evans R, Green T, Pritzel A, Ronneberger O, Willmore L, Ballard AJ, Bambrick J, Bodenstein SW, Evans DA, Hung C-C, O'Neill M, Reiman D, Tunyasuvunakool K, Wu Z, Žemgulytė A, Arvaniti E, Beattie C, Bertolli O, Bridgland A, Cherepanov A, Congreve M, Cowen-Rivers AI, Cowie A, Figurnov M, Fuchs FB, Gladman H, Jain R, Khan YA, Low CMR, Perlin K, Potapenko A, Savy P, Singh S, Stecula A, Thillaisundaram A, Tong C, Yakneen S, Zhong ED, Zielinski M, Žídek A, Bapst V, Kohli P, Jaderberg M, Hassabis D, Jumper JM. 2024. Accurate structure prediction of biomolecular interactions with AlphaFold 3. *Nature* 1–3. doi:10.1038/s41586-024-07487-w

Alexandrou AJ, Duncan RS, Sullivan A, Hancox JC, Leishman DJ, Witchel HJ, Leaney JL. 2006. Mechanism of hERG K+ channel blockade by the fluoroquinolone antibiotic moxifloxacin. *Br J Pharmacol* **147**:905–916. doi:10.1038/sj.bjp.0706678

AlQuraishi M. 2019. AlphaFold at CASP13. *Bioinforma Oxf Engl* **35**:4862–4865. doi:10.1093/bioinformatics/btz422

Asai T, Adachi N, Moriya T, Oki H, Maru T, Kawasaki M, Suzuki K, Chen S, Ishii R, Yonemori K, Igaki S, Yasuda S, Ogasawara S, Senda T, Murata T. 2021. Cryo-EM Structure of K+-Bound hERG Channel Complexed with the Blocker Astemizole. *Struct Lond Engl 1993* **29**:203-212.e4. doi:10.1016/j.str.2020.12.007

Baek M, DiMaio F, Anishchenko I, Dauparas J, Ovchinnikov S, Lee GR, Wang J, Cong Q, Kinch LN, Schaeffer RD, Millán C, Park H, Adams C, Glassman CR, DeGiovanni A, Pereira JH, Rodrigues AV, van Dijk AA, Ebrecht AC, Opperman DJ, Sagmeister T, Buhlheller C, Pavkov-Keller T, Rathinaswamy MK, Dalwadi U, Yip CK, Burke JE, Garcia KC, Grishin NV, Adams PD, Read RJ, Baker D. 2021. Accurate prediction of protein structures and interactions using a three-track neural network. *Science* **373**:871–876. doi:10.1126/science.abj8754

Beglov D, Roux B. 1994. Finite representation of an infinite bulk system: Solvent boundary potential for computer simulations. *J Chem Phys* **100**:9050–9063. doi:10.1063/1.466711

Berman HM, Westbrook J, Feng Z, Gilliland G, Bhat TN, Weissig H, Shindyalov IN, Bourne PE. 2000. The Protein Data Bank. *Nucleic Acids Res* **28**:235–242. doi:10.1093/nar/28.1.235

Branduardi D, Faraldo-Gómez JD. 2013. String method for calculation of minimum free-energy paths in Cartesian space in freely-tumbling systems. *J Chem Theory Comput* **9**:4140–4154. doi:10.1021/ct400469w

Brown BP, Stein RA, Meiler J, Mchaourab HS. 2024. Approximating Projections of Conformational Boltzmann Distributions with AlphaFold2 Predictions: Opportunities and Limitations. *J Chem Theory Comput*. doi:10.1021/acs.jctc.3c01081

Butler A, Helliwell MV, Zhang Y, Hancox JC, Dempsey CE. 2020. An Update on the Structure of hERG. *Front Pharmacol* **10**.

Butler A, Zhang Y, Stuart AG, Dempsey CE, Hancox JC. 2018. Action potential clamp characterization of the S631A hERG mutation associated with short QT syndrome. *Physiol Rep* **6**:e13845. doi:10.14814/phy2.13845

Cameron LP, Tombari RJ, Lu J, Pell AJ, Hurley ZQ, Ehinger Y, Vargas MV, McCarroll MN, Taylor JC, Myers-Turnbull D, Liu T, Yaghoobi B, Laskowski LJ, Anderson EI, Zhang G, Viswanathan J, Brown BM, Tjia M, Dunlap LE, Rabow ZT, Fiehn O, Wulff H, McCorvy JD, Lein PJ, Kokel D, Ron D, Peters J, Zuo Y, Olson DE. 2021. A Non-Hallucinogenic Psychedelic Analog with Therapeutic Potential. *Nature* **589**:474–479. doi:10.1038/s41586-020-3008-z

Case DA, Aktulga HM, Belfon K, Cerutti DS, Cisneros GA, Cruzeiro VWD, Forouzesh N, Giese TJ, Götz AW, Gohlke H, Izadi S, Kasavajhala K, Kaymak MC, King E, Kurtzman T, Lee T-S, Li P, Liu J, Luchko T, Luo R, Manathunga M, Machado MR, Nguyen HM, O'Hearn KA, Onufriev AV, Pan F, Pantano S, Qi R, Rahnamoun A, Risheh A, Schott-Verdugo S, Shajan A, Swails J, Wang J, Wei H, Wu X, Wu Y, Zhang S, Zhao

S, Zhu Q, Cheatham TEI, Roe DR, Roitberg A, Simmerling C, York DM, Nagan MC, Merz KMJr. 2023. AmberTools. *J Chem Inf Model* **63**:6183–6191. doi:10.1021/acs.jcim.3c01153

Case DA, Cheatham TE, Darden T, Gohlke H, Luo R, Merz KM, Onufriev A, Simmerling C, Wang B, Woods RJ. 2005. The Amber biomolecular simulation programs. *J Comput Chem* **26**:1668–1688. doi:10.1002/jcc.20290

Catterall WA, Wisedchaisri G, Zheng N. 2020. The Conformational Cycle of a Prototypical Voltage Gated Sodium Channel. *Nat Chem Biol* **16**:1314–1320. doi:10.1038/s41589-020-0644-4

Chandy KG, Sanches K, Norton RS. 2023. Structure of the voltage-gated potassium channel KV1.3: Insights into the inactivated conformation and binding to therapeutic leads. *Channels* **17**:2253104. doi:10.1080/19336950.2023.2253104

Chiu PJS, Marcoe KF, Bounds SE, Lin C-H, Feng J-J, Lin A, Cheng F-C, Crumb WJ, Mitchell R. 2004. Validation of a [3H]astemizole binding assay in HEK293 cells expressing HERG K+ channels. *J Pharmacol Sci* **95**:311–319. doi:10.1254/jphs.fpe0040101

Clarke CE, Hill AP, Zhao J, Kondo M, Subbiah RN, Campbell TJ, Vandenberg JI. 2006. Effect of S5P α-helix charge mutants on inactivation of hERG K+ channels. *J Physiol* **573**:291–304. doi:10.1113/jphysiol.2006.108332

Cordeiro JM, Brugada R, Wu YS, Hong K, Dumaine R. 2005. Modulation of IKr inactivation by mutation N588K in KCNH2: A link to arrhythmogenesis in short QT syndrome. *Cardiovasc Res* **67**:498–509. doi:10.1016/j.cardiores.2005.02.018

Cuello LG, Jogini V, Cortes DM, Perozo E. 2010. Structural mechanism of C-type inactivation in K+ channels. *Nature* **466**:203–208. doi:10.1038/nature09153

Darden T, York D, Pedersen L. 1993. Particle mesh Ewald: An N·log(N) method for Ewald sums in large systems. *J Chem Phys* **98**:10089–10092. doi:10.1063/1.464397

del Alamo D, Sala D, Mchaourab HS, Meiler J. 2022. Sampling alternative conformational states of transporters and receptors with AlphaFold2. *eLife* **11**:e75751. doi:10.7554/eLife.75751

DeMarco KR, Yang P-C, Singh V, Furutani K, Dawson JRD, Jeng M-T, Fettinger JC, Bekker S, Ngo VA, Noskov SY, Yarov-Yarovoy V, Sack JT, Wulff H, Clancy CE, Vorobyov I. 2021. Molecular determinants of pro-arrhythmia proclivity of d- and l-sotalol via a multi-scale modeling pipeline. *J Mol Cell Cardiol* **158**:163–177. doi:10.1016/j.yjmcc.2021.05.015

Doyle DA, Morais Cabral J, Pfuetzner RA, Kuo A, Gulbis JM, Cohen SL, Chait BT, MacKinnon R. 1998. The structure of the potassium channel: molecular basis of K+ conduction and selectivity. *Science* **280**:69–77. doi:10.1126/science.280.5360.69

Dun W, Jiang M, Tseng G-N. 1999. Allosteric effects of mutations in the extracellular S5-P loop on the gating and ion permeation properties of the hERG potassium channel. *Pflüg Arch* **439**:141–149. doi:10.1007/s004249900101

Fan JS, Jiang M, Dun W, McDonald TV, Tseng GN. 1999. Effects of outer mouth mutations on hERG channel function: a comparison with similar mutations in the Shaker channel. *Biophys J* **76**:3128–3140. doi:10.1016/S0006-3495(99)77464-3

Ferri N, Siegl P, Corsini A, Herrmann J, Lerman A, Benghozi R. 2013. Drug attrition during pre-clinical and clinical development: understanding and managing drug-induced cardiotoxicity. *Pharmacol Ther* **138**:470–484. doi:10.1016/j.pharmthera.2013.03.005

Ficker E, Jarolimek W, Kiehn J, Baumann A, Brown AM. 1998. Molecular determinants of dofetilide block of HERG K+ channels. *Circ Res* **82**:386–395. doi:10.1161/01.res.82.3.386

Fleishman SJ, Leaver-Fay A, Corn JE, Strauch E-M, Khare SD, Koga N, Ashworth J, Murphy P, Richter F, Lemmon G, Meiler J, Baker D. 2011. RosettaScripts: A Scripting Language Interface to the Rosetta Macromolecular Modeling Suite. *PLOS ONE* **6**:e20161. doi:10.1371/journal.pone.0020161

Goldschen-Ohm MP, Capes DL, Oelstrom KM, Chanda B. 2013. Multiple pore conformations driven by asynchronous movements of voltage sensors in a eukaryotic sodium channel. *Nat Commun* **4**:1350. doi:10.1038/ncomms2356

Gomis-Tena J, Brown BM, Cano J, Trenor B, Yang P-C, Saiz J, Clancy CE, Romero L. 2020. When Does the IC50 Accurately Assess the Blocking Potency of a Drug? *J Chem Inf Model* **60**:1779–1790. doi:10.1021/acs.jcim.9b01085

Gumbart J, Khalili-Araghi F, Sotomayor M, Roux B. 2012. Constant electric field simulations of the membrane potential illustrated with simple systems. *Biochim Biophys Acta BBA - Biomembr*, Membrane protein structure and function **1818**:294–302. doi:10.1016/j.bbamem.2011.09.030

Hansen RS, Diness TG, Christ T, Demnitz J, Ravens U, Olesen S-P, Grunnet M. 2006. Activation of human ether-a-go-go-related gene potassium channels by the diphenylurea 1,3-bis-(2-hydroxy-5-trifluoromethyl-phenyl)-urea (NS1643). *Mol Pharmacol* **69**:266–277. doi:10.1124/mol.105.015859

Helliwell MV, Zhang Y, El Harchi A, Du C, Hancox JC, Dempsey CE. 2018a. Structural implications of hERG K+ channel block by a high-affinity minimally structured blocker. *J Biol Chem* **293**:7040–7057. doi:10.1074/jbc.RA117.000363

Helliwell MV, Zhang Y, El Harchi A, Du C, Hancox JC, Dempsey CE. 2018b. Structural implications of hERG K+ channel block by a high-affinity minimally structured blocker. *J Biol Chem* **293**:7040–7057. doi:10.1074/jbc.RA117.000363

Hite RK, MacKinnon R. 2017. Structural Titration of Slo2.2, a Na+-Dependent K+ Channel. *Cell* **168**:390-399.e11. doi:10.1016/j.cell.2016.12.030

Huang J, Rauscher S, Nawrocki G, Ran T, Feig M, de Groot BL, Grubmüller H, MacKerell AD. 2017. CHARMM36m: an improved force field for folded and intrinsically disordered proteins. *Nat Methods* **14**:71–73. doi:10.1038/nmeth.4067

Huang P-S, Ban Y-EA, Richter F, Andre I, Vernon R, Schief WR, Baker D. 2011. RosettaRemodel: A Generalized Framework for Flexible Backbone Protein Design. *PLoS ONE* **6**:e24109. doi:10.1371/journal.pone.0024109

Humphrey W, Dalke A, Schulten K. 1996. VMD: visual molecular dynamics. *J Mol Graph* **14**:33–38, 27–28. doi:10.1016/0263-7855(96)00018-5

Jo S, Kim T, Iyer VG, Im W. 2008. CHARMM-GUI: A web-based graphical user interface for CHARMM. *J Comput Chem* **29**:1859–1865. doi:10.1002/jcc.20945

Johnson AA, Trudeau MC. 2023. Inhibition of hERG K channels by verapamil at physiological temperature: Implications for the CiPA Initiative. doi:10.1101/2023.12.12.571313

Jorgensen WL, Chandrasekhar J, Madura JD, Impey RW, Klein ML. 1983. Comparison of simple potential functions for simulating liquid water. *J Chem Phys* **79**:926–935. doi:10.1063/1.445869

Jumper J, Evans R, Pritzel A, Green T, Figurnov M, Ronneberger O, Tunyasuvunakool K, Bates R, Žídek A, Potapenko A, Bridgland A, Meyer C, Kohl SAA, Ballard AJ, Cowie A, Romera-Paredes B, Nikolov S, Jain R, Adler J, Back T, Petersen S, Reiman D, Clancy E, Zielinski M, Steinegger M, Pacholska M, Berghammer T, Bodenstein S, Silver D, Vinyals O, Senior AW, Kavukcuoglu K, Kohli P, Hassabis D. 2021a. Highly accurate protein structure prediction with AlphaFold. *Nature* **596**:583–589. doi:10.1038/s41586-021-03819-2

Jumper J, Evans R, Pritzel A, Green T, Figurnov M, Ronneberger O, Tunyasuvunakool K, Bates R, Žídek A, Potapenko A, Bridgland A, Meyer C, Kohl SAA, Ballard AJ, Cowie A, Romera-Paredes B, Nikolov S, Jain R, Adler J, Back T, Petersen S, Reiman D, Clancy E, Zielinski M, Steinegger M, Pacholska M, Berghammer T, Silver D, Vinyals O, Senior AW, Kavukcuoglu K, Kohli P, Hassabis D. 2021b. Applying and improving AlphaFold at CASP14. *Proteins* **89**:1711–1721. doi:10.1002/prot.26257

Kamiya K, Niwa R, Mitcheson JS, Sanguinetti MC. 2006. Molecular Determinants of hERG Channel Block. *Mol Pharmacol* **69**:1709–1716. doi:10.1124/mol.105.020990

Karelina M, Noh JJ, Dror RO. 2023. How accurately can one predict drug binding modes using AlphaFold models? *eLife* **12**:RP89386. doi:10.7554/eLife.89386

Kim S, Thiessen PA, Bolton EE, Chen J, Fu G, Gindulyte A, Han L, He J, He S, Shoemaker BA, Wang J, Yu B, Zhang J, Bryant SH. 2016. PubChem Substance and Compound databases. *Nucleic Acids Res* **44**:D1202-1213. doi:10.1093/nar/gkv951

Klauda JB, Venable RM, Freites JA, O'Connor JW, Tobias DJ, Mondragon-Ramirez C, Vorobyov I, MacKerell ADJr, Pastor RW. 2010. Update of the CHARMM All-Atom Additive Force Field for Lipids: Validation on Six Lipid Types. *J Phys Chem B* **114**:7830–7843. doi:10.1021/jp101759q

Kocadal K, Saygi S, Alkas FB, Sardas S. 2018. Drug-associated cardiovascular risks: A retrospective evaluation of withdrawn drugs. *North Clin Istanb* **6**:196–202. doi:10.14744/nci.2018.44977

Kushida S, Ogura T, Komuro I, Nakaya H. 2002. Inhibitory effect of the class III antiarrhythmic drug nifekalant on HERG channels: mode of action. *Eur J Pharmacol* **457**:19–27. doi:10.1016/s0014-2999(02)02666-3

Lam CK, de Groot BL. 2023. Ion Conduction Mechanisms in Potassium Channels Revealed by Permeation Cycles. *J Chem Theory Comput* **19**:2574–2589. doi:10.1021/acs.jctc.3c00061

Lane TJ. 2023. Protein structure prediction has reached the single-structure frontier. *Nat Methods* **20**:170–173. doi:10.1038/s41592-022-01760-4

Lau CHY, Flood E, Hunter MJ, Williams-Noonan BJ, Corbett KM, Ng C-A, Bouwer JC, Stewart AG, Perozo E, Allen TW, Vandenberg JI. 2024. Potassium dependent structural changes in the selectivity filter of HERG potassium channels. *Nat Commun* **15**:7470. doi:10.1038/s41467-024-51208-w

Lee S-Y, Kim Y-J, Kim K-T, Choe H, Jo S-H. 2006. Blockade of HERG human K+ channels and IKr of guinea-pig cardiomyocytes by the antipsychotic drug clozapine. *Br J Pharmacol* **148**:499–509. doi:10.1038/sj.bjp.0706744

Lees-Miller JP, Duan Y, Teng GQ, Duff HJ. 2000. Molecular determinant of high-affinity dofetilide binding to HERG1 expressed in Xenopus oocytes: involvement of S6 sites. *Mol Pharmacol* **57**:367–374.

Leman JK, Weitzner BD, Lewis SM, Adolf-Bryfogle J, Alam N, Alford RF, Aprahamian M, Baker D, Barlow KA, Barth P, Basanta B, Bender BJ, Blacklock K, Bonet J, Boyken SE, Bradley P, Bystroff C, Conway P, Cooper S, Correia BE, Coventry B, Das R, De Jong RM, DiMaio F, Dsilva L, Dunbrack R, Ford AS, Frenz B, Fu DY, Geniesse C, Goldschmidt L, Gowthaman R, Gray JJ, Gront D, Guffy S, Horowitz S, Huang P-S, Huber T, Jacobs TM, Jeliazkov JR, Johnson DK, Kappel K, Karanicolas J, Khakzad H, Khar KR, Khare SD, Khatib F, Khramushin A, King IC, Kleffner R, Koepnick B, Kortemme T, Kuenze G, Kuhlman B, Kuroda D, Labonte JW, Lai JK, Lapidoth G, Leaver-Fay A, Lindert S, Linsky T, London N, Lubin JH, Lyskov S, Maguire J, Malmström L, Marcos E, Marcu O, Marze NA, Meiler J, Moretti R, Mulligan VK, Nerli S, Norn C, Ó'Conchúir S, Ollikainen N, Ovchinnikov S, Pacella MS, Pan X, Park H, Pavlovicz RE, Pethe M, Pierce BG, Pilla KB, Raveh B, Renfrew PD, Burman SSR, Rubenstein A, Sauer MF, Scheck A, Schief W, Schueler-Furman O, Sedan Y, Sevy AM, Sgourakis NG, Shi L, Siegel JB, Silva D-A, Smith S, Song Y, Stein A, Szegedy M, Teets FD, Thyme SB, Wang RY-R, Watkins A, Zimmerman L, Bonneau R. 2020. Macromolecular modeling and design in Rosetta: recent methods and frameworks. *Nat Methods* **17**:665–680. doi:10.1038/s41592-020-0848-2

Li J, Shen R, Reddy B, Perozo E, Roux B. 2021. Mechanism of C-type inactivation in the hERG potassium channel. *Sci Adv* **7**:eabd6203. doi:10.1126/sciadv.abd6203

Li M, Ramos LG. 2017. Drug-Induced QT Prolongation And Torsades de Pointes. *Pharm Ther* **42**:473–477.

Li P, Sun H, Zhou P, Ma C, Hu G, Jiang H, Li M, Liu H, Gao Z. 2012. Comparison of the effects of DC031050, a class III antiarrhythmic agent, on hERG channel and three neuronal potassium channels. *Acta Pharmacol Sin* **33**:728–736. doi:10.1038/aps.2012.41

Li Z, Wu Q, Huang G, Jin X, Li J, Pan X, Yan N. 2024. Dissection of the structure-function relationship of Nav channels. *Proc Natl Acad Sci U S A* **121**:e2322899121. doi:10.1073/pnas.2322899121

Lin Z, Akin H, Rao R, Hie B, Zhu Z, Lu W, Smetanin N, Verkuil R, Kabeli O, Shmueli Y, dos Santos Costa A, Fazel-Zarandi M, Sercu T, Candido S, Rives A. 2023. Evolutionary-scale prediction of atomic-level protein structure with a language model. *Science* **379**:1123–1130. doi:10.1126/science.ade2574

Liu J, Zhang M, Jiang M, Tseng G-N. 2002. Structural and Functional Role of the Extracellular S5-P Linker in the HERG Potassium Channel. *J Gen Physiol* **120**:723–737. doi:10.1085/jgp.20028687

Long SB, Campbell EB, Mackinnon R. 2005. Crystal structure of a mammalian voltage-dependent Shaker family K+ channel. *Science* **309**:897–903. doi:10.1126/science.1116269

Maly J, Emigh AM, DeMarco KR, Furutani K, Sack JT, Clancy CE, Vorobyov I, Yarov-Yarovoy V. 2022. Structural modeling of the hERG potassium channel and associated drug interactions. *Front Pharmacol* **13**:966463. doi:10.3389/fphar.2022.966463

Mandala VS, MacKinnon R. 2022. Voltage-sensor movements in the Eag Kv channel under an applied electric field. *Proc Natl Acad Sci U S A* **119**:e2214151119. doi:10.1073/pnas.2214151119

Miao Y, Bhattarai A, Wang J. 2020. Ligand Gaussian accelerated molecular dynamics (LiGaMD): Characterization of ligand binding thermodynamics and kinetics. *J Chem Theory Comput* **16**:5526–5547. doi:10.1021/acs.jctc.0c00395

Miranda WE, DeMarco KR, Guo J, Duff HJ, Vorobyov I, Clancy CE, Noskov SYu. 2020. Selectivity filter modalities and rapid inactivation of the hERG1 channel. *Proc Natl Acad Sci* **117**:2795–2804. doi:10.1073/pnas.1909196117

Mirdita M, Schütze K, Moriwaki Y, Heo L, Ovchinnikov S, Steinegger M. 2022. ColabFold: making protein folding accessible to all. *Nat Methods* **19**:679–682. doi:10.1038/s41592-022-01488-1

Mirdita M, Steinegger M, Söding J. 2019. MMseqs2 desktop and local web server app for fast, interactive sequence searches. *Bioinforma Oxf Engl* **35**:2856–2858. doi:10.1093/bioinformatics/bty1057

Nakajima T, Furukawa T, Tanaka T, Katayama Y, Nagai R, Nakamura Y, Hiraoka M. 1998. Novel Mechanism of HERG Current Suppression in LQT2. *Circ Res* **83**:415–422. doi:10.1161/01.RES.83.4.415

Noel JK, Whitford PC, Onuchic JN. 2012. The Shadow Map: A General Contact Definition for Capturing the Dynamics of Biomolecular Folding and Function. *J Phys Chem B* **116**:8692–8702. doi:10.1021/jp300852d

Numaguchi H, Mullins FM, Johnson JP, Johns DC, Po SS, Yang IC-H, Tomaselli GF, Balser JR. 2000. Probing the Interaction Between Inactivation Gating and dd-Sotalol Block of HERG. *Circ Res* **87**:1012–1018. doi:10.1161/01.RES.87.11.1012

Orvos P, Kohajda Z, Szlovák J, Gazdag P, Árpádffy-Lovas T, Tóth D, Geramipour A, Tálosi L, Jost N, Varró A, Virág L. 2019. Evaluation of Possible Proarrhythmic Potency: Comparison of the Effect of Dofetilide, Cisapride, Sotalol, Terfenadine, and Verapamil on hERG and Native IKr Currents and on Cardiac Action Potential. *Toxicol Sci Off J Soc Toxicol* **168**:365–380. doi:10.1093/toxsci/kfy299

Park H, Zhou G, Baek M, Baker D, DiMaio F. 2021. Force Field Optimization Guided by Small Molecule Crystal Lattice Data Enables Consistent Sub-Angstrom Protein-Ligand Docking. *J Chem Theory Comput* **17**:2000–2010. doi:10.1021/acs.jctc.0c01184

Paul AA, Witchel HJ, Hancox JC. 2002. Inhibition of the current of heterologously expressed HERG potassium channels by flecainide and comparison with quinidine, propafenone and lignocaine. *Br J Pharmacol* **136**:717–729. doi:10.1038/sj.bjp.0704784

Perrin MJ, Kuchel PW, Campbell TJ, Vandenberg JI. 2008. Drug Binding to the Inactivated State Is Necessary but Not Sufficient for High-Affinity Binding to Human Ether-à-go-go-Related Gene Channels. *Mol Pharmacol* **74**:1443–1452. doi:10.1124/mol.108.049056

Pettersen EF, Goddard TD, Huang CC, Meng EC, Couch GS, Croll TI, Morris JH, Ferrin TE. 2021. UCSF ChimeraX: Structure visualization for researchers, educators, and developers. *Protein Sci Publ Protein Soc* **30**:70–82. doi:10.1002/pro.3943

Pettini F, Domene C, Furini S. 2023. Early Steps in C-Type Inactivation of the hERG Potassium Channel. *J Chem Inf Model* **63**:251–258. doi:10.1021/acs.jcim.2c01028

Phartiyal P, Jones EMC, Robertson GA. 2007. Heteromeric Assembly of Human Ether-à-go-go-related Gene (hERG) 1a/1b Channels Occurs Cotranslationally via N-terminal Interactions*. *J Biol Chem* **282**:9874–9882. doi:10.1074/jbc.M610875200

Pirok G, Maté N, Varga J, Szegezdi J, Vargyas M, Dórant S, Csizmadia F. 2006. Making "real" molecules in virtual space. *J Chem Inf Model* **46**:563–568. doi:10.1021/ci050373p

Priest B, Bell IM, Garcia M. 2008. Role of hERG potassium channel assays in drug development. *Channels* **2**:87–93. doi:10.4161/chan.2.2.6004

Rampe D, Roy ML, Dennis A, Brown AM. 1997. A mechanism for the proarrhythmic effects of cisapride (Propulsid): high affinity blockade of the human cardiac potassium channel HERG. *FEBS Lett* **417**:28–32. doi:10.1016/s0014-5793(97)01249-0

Romero L, Trenor B, Yang P-C, Saiz J, Clancy CE. 2015. In silico screening of the impact of hERG channel kinetic abnormalities on channel block and susceptibility to acquired long QT syndrome. *J Mol Cell Cardiol* **87**:271–282. doi:10.1016/j.yjmcc.2015.08.015

Roux B. 2017. Ion channels and ion selectivity. *Essays Biochem* **61**:201–209. doi:10.1042/EBC20160074

Ryckaert J-P, Ciccotti G, Berendsen HJC. 1977. Numerical integration of the cartesian equations of motion of a system with constraints: molecular dynamics of n-alkanes. *J Comput Phys* **23**:327–341. doi:10.1016/0021-9991(77)90098-5

Sala D, Hildebrand PW, Meiler J. 2023. Biasing AlphaFold2 to predict GPCRs and kinases with user-defined functional or structural properties. *Front Mol Biosci* **10**:1121962. doi:10.3389/fmolb.2023.1121962

Salentin S, Schreiber S, Haupt VJ, Adasme MF, Schroeder M. 2015. PLIP: fully automated protein–ligand interaction profiler. *Nucleic Acids Res* **43**:W443–W447. doi:10.1093/nar/gkv315

Sănchez-Chapula JA, Ferrer T, Navarro-Polanco RA, Sanguinetti MC. 2003. Voltage-dependent profile of human ether-a-go-go-related gene channel block is influenced by a single residue in the S6 transmembrane domain. *Mol Pharmacol* **63**:1051–1058. doi:10.1124/mol.63.5.1051

Sanguinetti MC, Tristani-Firouzi M. 2006. hERG potassium channels and cardiac arrhythmia. *Nature* **440**:463–469. doi:10.1038/nature04710

Satler CA, Vesely MR, Duggal P, Ginsburg GS, Beggs AH. 1998. Multiple different missense mutations in the pore region of HERG in patients with long QT syndrome. *Hum Genet* **102**:265–272. doi:10.1007/s004390050690

Saxena P, Zangerl-Plessl E-M, Linder T, Windisch A, Hohaus A, Timin E, Hering S, Stary-Weinzinger A. 2016. New potential binding determinant for hERG channel inhibitors. *Sci Rep* **6**:24182. doi:10.1038/srep24182

Schönherr R, Heinemann SH. 1996. Molecular determinants for activation and inactivation of HERG, a human inward rectifier potassium channel. *J Physiol* **493**:635–642. doi:10.1113/jphysiol.1996.sp021410

Selvakumar P, Fernández-Mariño AI, Khanra N, He C, Paquette AJ, Wang B, Huang R, Smider VV, Rice WJ, Swartz KJ, Meyerson JR. 2022. Structures of the T cell potassium channel Kv1.3 with immunoglobulin modulators. *Nat Commun* **13**:3854. doi:10.1038/s41467-022-31285-5

Shi YP, Thouta S, Claydon TW. 2020. Modulation of hERG K+ Channel Deactivation by Voltage Sensor Relaxation. *Front Pharmacol* **11**. doi:10.3389/fphar.2020.00139

Stepanovic SZ, Potet F, Petersen CI, Smith JA, Meiler J, Balser JR, Kupershmidt S. 2009. The evolutionarily conserved residue A653 plays a key role in HERG channel closing. *J Physiol* **587**:2555–2566. doi:10.1113/jphysiol.2008.166694

Stork D, Timin EN, Berjukow S, Huber C, Hohaus A, Auer M, Hering S. 2007. State dependent dissociation of HERG channel inhibitors. *Br J Pharmacol* **151**:1368–1376. doi:10.1038/sj.bjp.0707356

Suessbrich H, Schönherr R, Heinemann SH, Attali B, Lang F, Busch AE. 1997. The inhibitory effect of the antipsychotic drug haloperidol on HERG potassium channels expressed in Xenopus oocytes. *Br J Pharmacol* **120**:968–974. doi:10.1038/sj.bjp.0700989

Tan X-F, Bae C, Stix R, Fernández-Mariño AI, Huffer K, Chang T-H, Jiang J, Faraldo-Gómez JD, Swartz KJ. 2022. Structure of the Shaker Kv channel and mechanism of slow C-type inactivation. *Sci Adv* **8**:eabm7814. doi:10.1126/sciadv.abm7814

Tanaka H, Takahashi Y, Hamaguchi S, Iida-Tanaka N, Oka T, Nishio M, Ohtsuki A, Namekata I. 2014. Effect of Terfenadine and Pentamidine on the hERG Channel and Its Intracellular Trafficking: Combined Analysis with Automated Voltage Clamp and Confocal Microscopy. *Biol Pharm Bull* **37**:1826–1830. doi:10.1248/bpb.b14-00417

Thouta S, Sokolov S, Abe Y, Clark SJ, Cheng YM, Claydon TW. 2014. Proline Scan of the hERG Channel S6 Helix Reveals the Location of the Intracellular Pore Gate. *Biophys J* **106**:1057–1069. doi:10.1016/j.bpj.2014.01.035

Tingle BI, Tang KG, Castanon M, Gutierrez JJ, Khurelbaatar M, Dandarchuluun C, Moroz YS, Irwin JJ. 2023. ZINC-22—A Free Multi-Billion-Scale Database of Tangible Compounds for Ligand Discovery. *J Chem Inf Model* **63**:1166–1176. doi:10.1021/acs.jcim.2c01253

Tyagi A, Ahmed T, Jian S, Bajaj S, Ong ST, Goay SSM, Zhao Y, Vorobyov I, Tian C, Chandy KG, Bhushan S. 2022. Rearrangement of a unique Kv1.3 selectivity filter conformation upon binding of a drug. *Proc Natl Acad Sci U S A* **119**:e2113536119. doi:10.1073/pnas.2113536119

Vandenberg JI, Perry MD, Perrin MJ, Mann SA, Ke Y, Hill AP. 2012. hERG K(+) channels: structure, function, and clinical significance. *Physiol Rev* **92**:1393–1478. doi:10.1152/physrev.00036.2011

Varadi M, Velankar S. 2023. The impact of AlphaFold Protein Structure Database on the fields of life sciences. *Proteomics* **23**:e2200128. doi:10.1002/pmic.202200128

Waldo AL, Camm AJ, deRuyter H, Friedman PL, MacNeil DJ, Pauls JF, Pitt B, Pratt CM, Schwartz PJ, Veltri EP. 1996. Effect of d-sotalol on mortality in patients with left ventricular dysfunction after recent and remote myocardial infarction. *The Lancet* **348**:7–12. doi:10.1016/S0140-6736(96)02149-6

Walker BD, Valenzuela SM, Singleton CB, Tie H, Bursill JA, Wyse KR, Qiu MR, Breit SN, Campbell TJ. 1999. Inhibition of HERG channels stably expressed in a mammalian cell line by the antianginal agent perhexiline maleate. *Br J Pharmacol* **127**:243–251. doi:10.1038/sj.bjp.0702502

Wang S, Morales MJ, Liu S, Strauss HC, Rasmusson RL. 1997. Modulation of HERG affinity for E-4031 by [K+]o and C-type inactivation. *FEBS Lett* **417**:43–47. doi:10.1016/S0014-5793(97)01245-3

Wang W, MacKinnon R. 2017. Cryo-EM Structure of the Open Human Ether-à-go-go-Related K+ Channel hERG. *Cell* **169**:422-430.e10. doi:10.1016/j.cell.2017.03.048

Windisch A, Timin EN, Schwarz T, Stork-Riedler D, Erker T, Ecker GF, Hering S. 2011. Trapping and dissociation of propafenone derivatives in HERG channels. *Br J Pharmacol* **162**:1542. doi:10.1111/j.1476-5381.2010.01159.x

Windley MJ, Abi-Gerges N, Fermini B, Hancox JC, Vandenberg JI, Hill AP. 2017. Measuring kinetics and potency of hERG block for CiPA. *J Pharmacol Toxicol Methods*, Focused Issue on Safety Pharmacology **87**:99–107. doi:10.1016/j.vascn.2017.02.017

Wu Y, Yan Y, Yang Y, Bian S, Rivetta A, Allen K, Sigworth FJ. 2023. Cryo-EM structures of Kv1.2 potassium channels, conducting and non-conducting. *eLife* **12**. doi:10.7554/eLife.89459.1

Yan M, Fan P, Shi Y, Feng L, Wang J, Zhan G, Li B. 2016. Stereoselective Blockage of Quinidine and Quinine in the hERG Channel and the Effect of Their Rescue Potency on Drug-Induced hERG Trafficking Defect. *Int J Mol Sci* **17**. doi:10.3390/ijms17101648

Yang P-C, DeMarco KR, Aghasafari P, Jeng M-T, Dawson JRD, Bekker S, Noskov SY, Yarov-Yarovoy V, Vorobyov I, Clancy CE. 2020. A Computational Pipeline to Predict Cardiotoxicity: From the Atom to the Rhythm. *Circ Res* **126**:947–964. doi:10.1161/CIRCRESAHA.119.316404

Yao X, Gao S, Yan N. 2023. Structural biology of voltage-gated calcium channels. *Channels* **18**:2290807. doi:10.1080/19336950.2023.2290807

Zhang S, Zhou Z, Gong Q, Makielski JC, January CT. 1999. Mechanism of block and identification of the verapamil binding domain to HERG potassium channels. *Circ Res* **84**:989–998. doi:10.1161/01.res.84.9.989

Zhang Y, Colenso CK, El Harchi A, Cheng H, Witchel HJ, Dempsey CE, Hancox JC. 2016. Interactions between amiodarone and the hERG potassium channel pore determined with mutagenesis and in silico docking. *Biochem Pharmacol* **113**:24–35. doi:10.1016/j.bcp.2016.05.013

Zhao JT, Hill AP, Varghese A, Cooper AA, Swan H, Laitinen-Forsblom PJ, Rees MI, Skinner JR, Campbell TJ, Vandenberg JI. 2009. Not all hERG pore domain mutations have a severe phenotype: G584S has an inactivation gating defect with mild phenotype compared to G572S, which has a dominant negative trafficking defect and a severe phenotype. *J Cardiovasc Electrophysiol* **20**:923–930. doi:10.1111/j.1540-8167.2009.01468.x

Zhou Z, Gong Q, Ye B, Fan Z, Makielski JC, Robertson GA, January CT. 1998. Properties of HERG channels stably expressed in HEK 293 cells studied at physiological temperature. *Biophys J* **74**:230–241.

Tables

Table 1. Criteria for different type of non-bonded interactions used in analyses

Types of interaction	Detection criteria	Filtering criteria
Hydrogen Bonds	Distance between the hydrogen bond donor (D) and acceptor (A) should be less than 3.8 Å. The angle D-H···A should be above 110°.	Exclude hydrogen bonds between atoms that already form a salt bridge. A hydrogen bond donor can participate in only one hydrogen bond, while acceptor atoms can form multiple hydrogen bonds.
Salt Bridges	Geometric centers of oppositely charged groups that come within 4.5 Å.	
Cation-π	Pairing of a positive charge and an aromatic ring if the distance between the charge center and the aromatic ring center is less than 6 Å.	
π-Stacking	Geometric centers of two aromatic rings within 5.5 Å. The angle between the rings should deviate no more than 30° from the optimal angle (90° for T-stacking, 180° for P-stacking). When projecting each ring center onto the opposite ring plane, the distance between the other ring center and the projected point (offset) should be less than 2 Å.	

Table 2. Mutations known to affect hERG channel inactivation.

Mutation(s)	Reported impact on hERG channel	References
N629D, N629S, N633S	Disrupt inactivation and K^+ selectivity	(Miranda et al., 2020; Satler et al., 1998)
H587P/K	Disrupts C-type inactivation and K^+ selectivity	(Dun et al., 1999)
S631A	Causes positive shift in half-inactivation voltage	(Butler et al., 2018)
S631C	Speeds up fast inactivation	(Fan et al., 1999)
N588K/E, Q592K	Modulate rapid inactivation	(Clarke et al., 2006; Cordeiro et al., 2005)
D591R/Q592R	Inhibit inactivation	(Clarke et al., 2006)
G584S	Leads to inactivation gating defects	(Zhao et al., 2009)
S620T	Abolishes hERG inactivation	(Ficker et al., 1998)
V630L	Causes negative shift in steady-state inactivation	(Nakajima et al., 1998)
N588C, I583C	High and intermediate impact on hERG inactivation	(Liu et al., 2002)

Table 3. Data used for validating binding affinities from drug docking simulation with experiments

Drugs	Ionization states & prevalence at pH 7.4	Simulated binding affinities (Rosetta Energy Units)			hERG channel state distribution when the tail current was observed			$\Delta G_{bind,\,sim}$ (Rosetta Energy Units)	$\Delta G_{bind,\,exp}$ (kcal/mol)	IC_{50} (nM)	Studies referenced
		Open	Inact.	Closed	Open	Inact.	Closed				
astemizole	Neutral 1.51%*	-11.88 ± 0.47	-25.08 ± 1.46	-17.83 ± 0.99	43.96%	52.43%	3.61%	-25.16 ± 1.66	-4.67	26	(Chiu et al., 2004)
	Cationic 98.50%*	-17.91 ± 3.49	-31.58 ± 1.30	-22.78 ± 4.06							
terfenadine	Neutral 1.50%	-21.00 ± 1.11	-27.23 ± 1.52	-25.90 ± 1.74	45.21%; 57.91%	53.93%; 40.71%	0.86%; 1.38%	-29.76 ± 0.34; -27.67 ± 0.34	-4.63; -4.63	31; 30.6	(Orvos et al., 2019); (Tanaka et al., 2014)
	Neutral 98.50%	-22.49 ± 0.50	-36.01 ± 0.47	-29.28 ± 2.31							
cisapride	Neutral 22.40%	-9.85 ± 0.37	-20.85 ± 1.21	-12.98 ± 3.29	41.89%; 43.96%	51.15%; 52.43%	6.96%; 3.61%	-19.40 ± 0.55; -19.53 ± 0.52	-4.31; -5.03	44.5; 6.9	(Rampe et al., 1997); (Chiu et al., 2004)
	Cationic 77.60%	-13.02 ± 0.60	-27.45 ± 1.06	-14.06 ± 4.59							
verapimil	Neutral 0.60%	-14.68 ± 1.72	-18.37 ± 1.19	-20.17 ± 1.09	56.98%; 9.00%	40.07%; 90.62%	2.94%; 0.38%	-20.21 ± 1.29; -26.08 ± 2.65	-4.01; -4.15	143; 180.4	(Zhang et al., 1999); (Johnson and Trudeau, 2023)
	Cationic 99.40%	-15.13 ± 0.96	-27.23 ± 2.94	-23.69 ± 1.57							
d-sotalol	Neutral 0.62%*	-5.48 ± 0.56	-9.09 ± 1.11	-9.54 ± 0.57	91.54%	4.50%	3.96%	-6.59 ± 0.80	-2.03	515,500	(Perrin et al., 2008)
	Cationic 99.38%*	-6.15 ± 0.88	-12.50 ± 1.59	-10.09 ± 0.35							
l-sotalol	Neutral 0.62%*	-5.19 ± 0.62	-10.11 ± 0.80	-9.55 ± 0.54	91.54%	4.50%	3.96%	-4.55 ± 1.13	-2.03	515,500	(Perrin et al., 2008)
	Cationic 99.38%*	-3.89 ± 1.24	-11.49 ± 1.75	-11.67 ± 0.93							
dofetilide	Neutral 5.70%	-4.85 ± 1.22	-10.35 ± 1.66	-4.05 ± 1.58	19.23%; 57.04%	77.68%; 40.14%	3.08%; 2.83%	-15.71 ± 0.93; -12.62 ± 0.91	-3.81; -4.31	320; 17.90	(Ficker et al., 1998); (Li et al., 2012)
	Cationic 94.30%	-9.07 ± 1.46	-18.14 ± 1.21	-4.99 ± 1.45							
haloperidol	Neutral 15.50%	-10.97 ± 0.11	-20.23 ± 0.74	-15.61 ± 1.18	54.25%	13.37%	32.38%	-15.08 ± 0.40	-3.52	1,000	(Suessbrich et al., 1997)
	Cationic 84.50%	-11.27 ± 0.07	-24.21 ± 0.71	-18.48 ± 1.41							
amiodarone	Neutral 2.00%	-8.95 ± 1.18	-27.08 ± 1.36	-9.28 ± 1.85	45.21%	53.93%	0.86%	-20.64 ± 1.05	-4.53	45	(Zhang et al., 2016)
	Cationic 98.00%	-10.42 ± 1.69	-29.40 ± 1.38	-13.08 ± 4.03							
E-4031	Neutral 21.09%*	-9.48 ± 0.14	-17.87 ± 2.23	-6.10 ± 1.01	57.70%	40.54%	1.76%	-14.41 ± 0.62	-5.00	7.7	(Zhou et al., 1998)
	Cationic 78.91%*	-11.22 ± 0.36	-20.15 ± 1.78	-10.89 ± 1.89							
clozapine	Neutral 100%*	-7.97 ± 0.37	-13.94 ± 0.19	-13.96 ± 0.35	62.12%; 67.97%	25.62%; 27.99%	12.27%; 4.05%	-10.23 ± 0.24; -9.88 ± 0.26	-2.67; -2.72	28,300; 22,900	(Lee et al., 2006)
NS1643	Neutral 100%*	-10.66 ± 0.56	-19.88 ± 0.75	-19.18 ± 1.22	69.21%	28.79%	2.00%	-13.49 ± 0.44	-3.07	10,500	(Hansen et al., 2006)

moxifloxacin	Neutral 0%	-3.25 ± 1.89	-11.80 ± 0.88	-17.95 ± 1.67	34.82%; 45.21%	42.72%; 53.93%	22.46%; 0.86%	-9.57 ± 0.6; -10.19 ± 0.33	-2.45; -2.74	65,000; 35,700	(Alexandrou et al., 2006)
	Zwitterionic 100%*	-9.35 ± 0.01	-10.94 ± 0.61	-7.32 ± 2.42							
quinidine	Neutral 2.20%	-7.16 ± 0.81	-9.36 ± 0.86	-13.23 ± 0.19	57.17%; 32.84%	23.59%; 66.68%	19.24%; 0.48%	-10.86 ± 0.16; -9.78 ± 0.43	-3.57; -3.93	800; 410	(Yan et al., 2016); (Paul et al., 2002)
	Cationic 97.70%	-9.38 ± 0.08	-9.98 ± 0.66	-16.63 ± 0.19							
perhexiline	Neutral 0%	-10.15 ± 0.59	-6.28 ± 0.71	-20.92 ± 0.83	37.57%	60.59%	1.84%	-7.55 ± 0.30	-2.99	7,800	(Walker et al., 1999)
	Cationic 100%	-11.54 ± 0.56	-4.66 ± 0.36	-21.50 ± 1.67							
nifekalant	Neutral 3.80%	-7.68 ± 0.92	-15.67 ± 0.97	-11.86 ± 1.53	67.65%	27.91%	4.44%	-12.77 ± 0.75	-2.99	7,900	(Kushida et al., 2002)
	Cationic 96.20%	-9.33 ± 1.05	-21.31 ± 1.13	-13.90 ± 1.47							
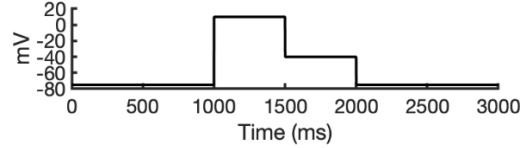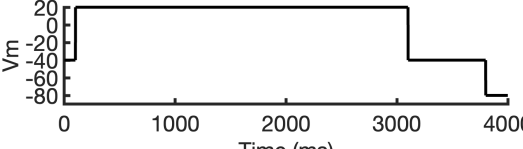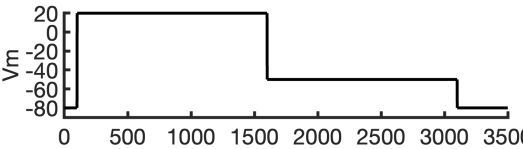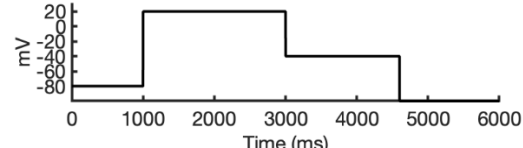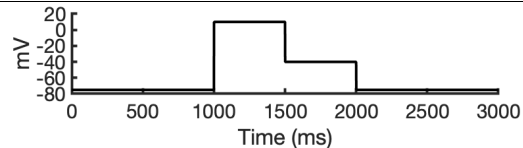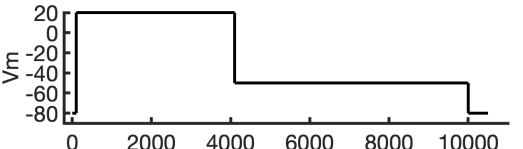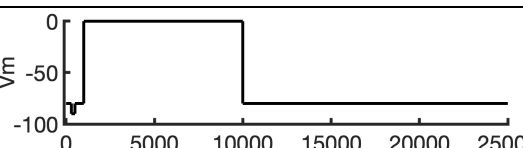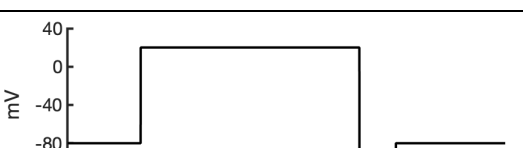
In the *Ionization states* column, the microspecies distribution percentages were calculated using the ChemAxon software suite (Pirok et al., 2006). The asterisk (*) indicates that the value has been adjusted by a few percentages to account for species with alternate ionization states that were not tested.
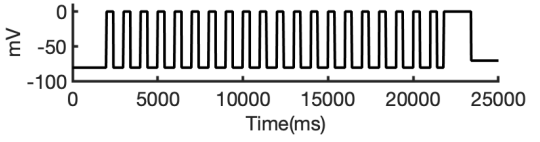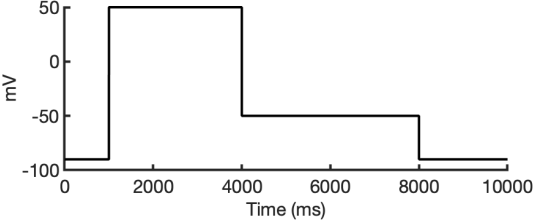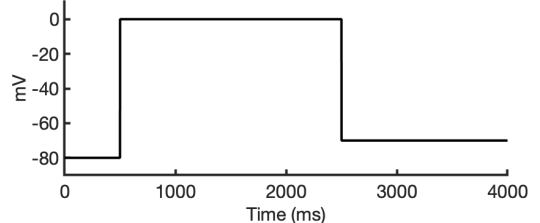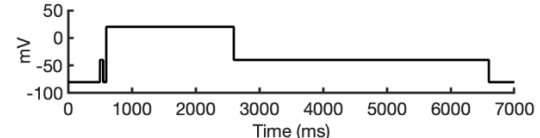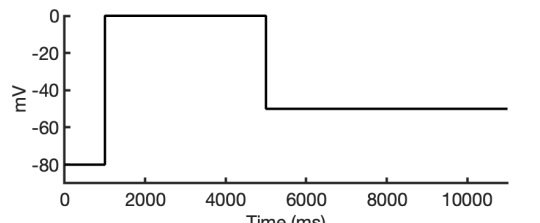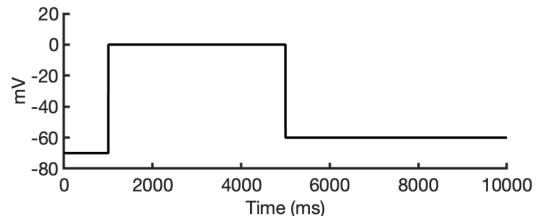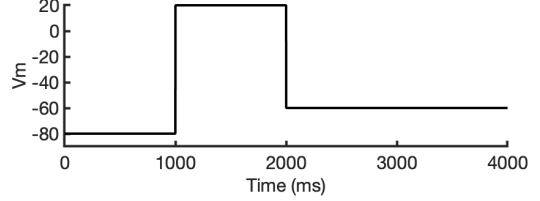
Table 4. Transition rates in the hERG channel (I_{Kr}) Markov model
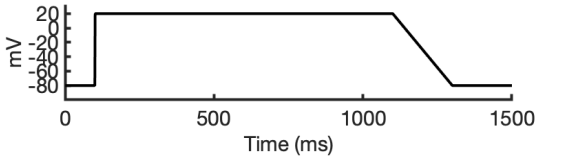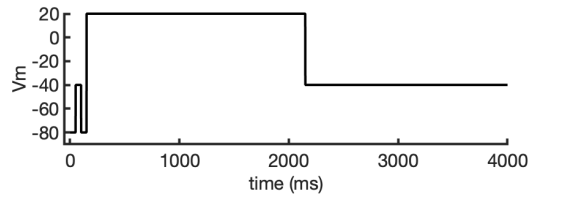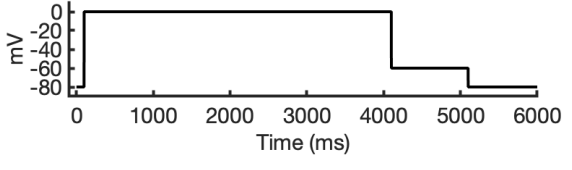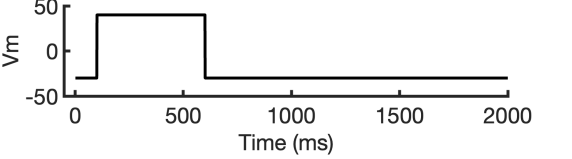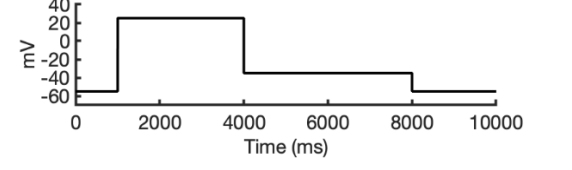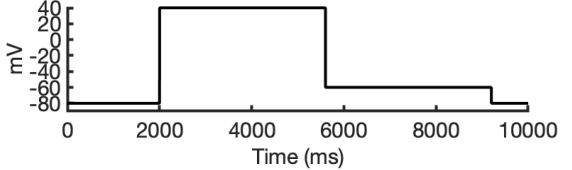
Transition rates (ms^{-1}) _Drug free Kr channel_	
C3→C2	$ae = \dfrac{T}{T_{base}} e^{\left(24.335 + \frac{T_{base}}{T}(0.0112 \times V - 25.914)\right)}$
C2→C3	$be = \dfrac{T}{T_{base}} e^{\left(13.688 + \frac{T_{base}}{T}(-0.0603 \times V - 15.707)\right)}$
C2→C1	$ain = \dfrac{T}{T_{base}} e^{\left(22.746 + \frac{T_{base}}{T}(-25.914)\right)}$
C1→C2	$bin = \dfrac{T}{T_{base}} e^{\left(13.193 + \frac{T_{base}}{T}(-15.707)\right)}$
C1→O	$aa = \dfrac{T}{T_{base}} e^{\left(22.098 + \frac{T_{base}}{T}(0.0365 \times V - 25.914)\right)}$
O→C1	$bb = \dfrac{T}{T_{base}} e^{\left(7.313 + \frac{T_{base}}{T}(-0.0399 \times V - 15.707)\right)}$
O→I	$\beta i = \dfrac{T}{T_{base}} e^{\left(30.016 + \frac{T_{base}}{T}(0.0223 \times V - 30.88)\right)} \times \left(\dfrac{5.4}{[K]^o}\right)^{0.4}$
I→O	$\alpha i = \dfrac{T}{T_{base}} e^{\left(30.061 + \frac{T_{base}}{T}(-0.0312 \times V - 33.243)\right)}$
T_{base}	310 K
T	Please see **Table 4**

Table 5. Voltage stimulation protocols and IC$_{50}$ for drugs used in the model

Drugs	IC$_{50}$ (nM)	Dose (nM)	Temperature (K)	Voltage protocols	Refs
astemizole	26	80	310		(Chiu et al., 2004)
terfenadine	31	100	310		(Orvos et al., 2019)
	30.6	30	310		(Tanaka et al., 2014)
cisapride	44.5	100	295		(Rampe et al., 1997)
	6.9	20	310		(Chiu et al., 2004)
verapimil	143	500	295		(Zhang et al., 1999)
	180.4	300	310		(Johnson and Trudeau, 2023)
dl-sotalol	515,500	300,000	310		(Perrin et al., 2008)

31

dofetilide	320	1,000	295		(Ficker et al., 1998)
	17.9	10	295		(Li et al., 2012)
haloperidol	1,000	3,000	295		(Suessbrich et al., 1997)
amiodarone	45	100	310		(Zhang et al., 2016)
E-4031	7.7	10	310		(Zhou et al., 1998)
clozapine	28,300	20,000	295		(Lee et al., 2006)
	22,900	20,000	295		
NS1643	10,500	30,000	310		(Hansen et al., 2006)

moxifloxacin	65,000	60,000	295		(Alexandrou et al., 2006)
	35,700	600,000	310		
quinidine	800	500	295		(Yan et al., 2016)
	410	500	310		(Paul et al., 2002)
perhexiline	7,800	1,000	295		(Walker et al., 1999)
nifekalant	7,900	1,000	295		(Kushida et al., 2002)

Main Figures
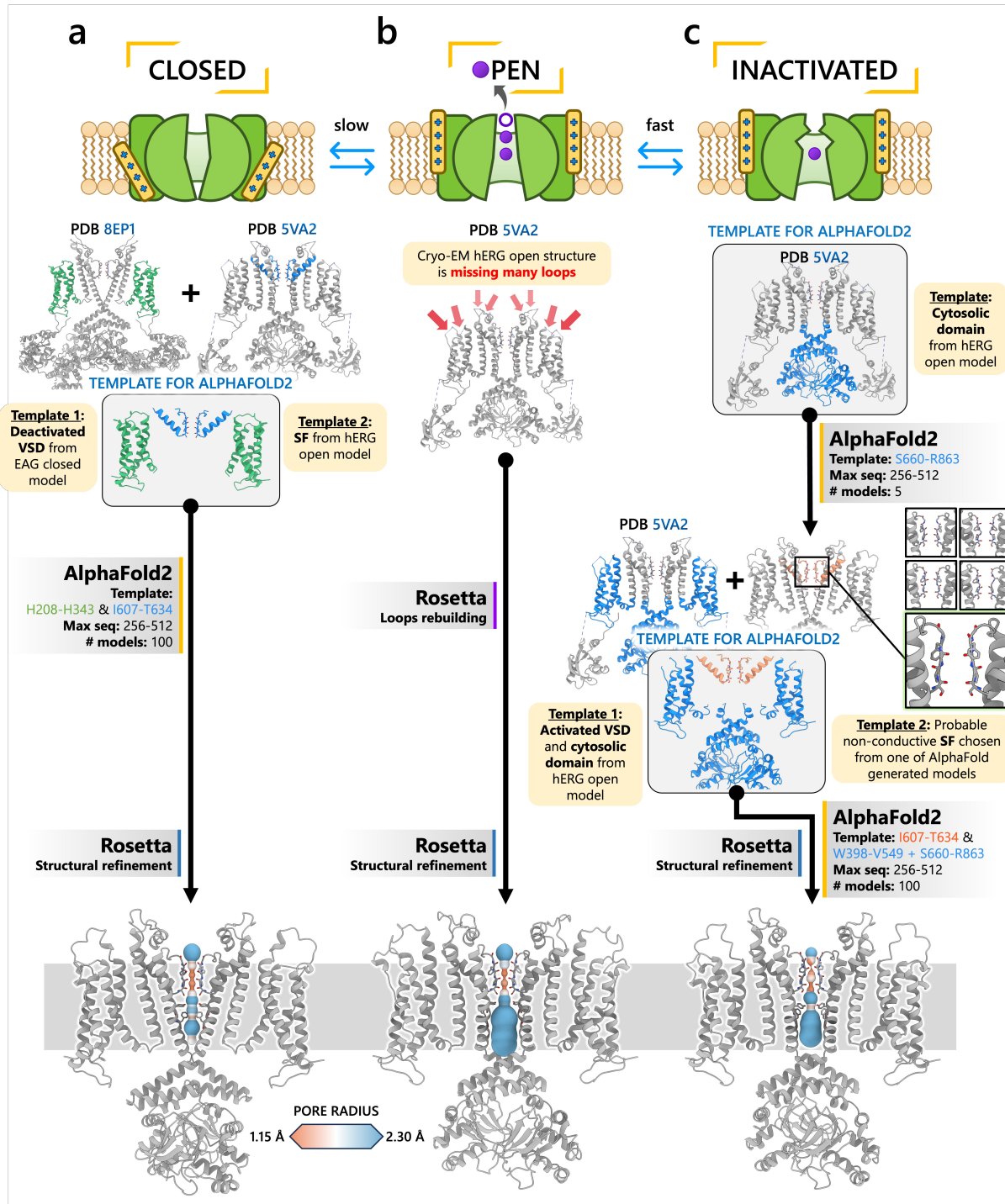
Figure 1. Generation of hERG channel models in the closed (a), open (b), and inactivated (c) states. The lower limit of the pore radius color profile (1.15 Å) indicates the minimum radius to accommodate a water molecule, and the upper limit (2.30 Å) indicates sufficient space to fit two water molecules side-by-side. "Max seq" is a setting in ColabFold that denotes the maximum number of cluster centers and extra sequences that the MSA used for AlphaFold2 will be subsampled to. "# models" indicates the number of models predicted using the provided structural templates.
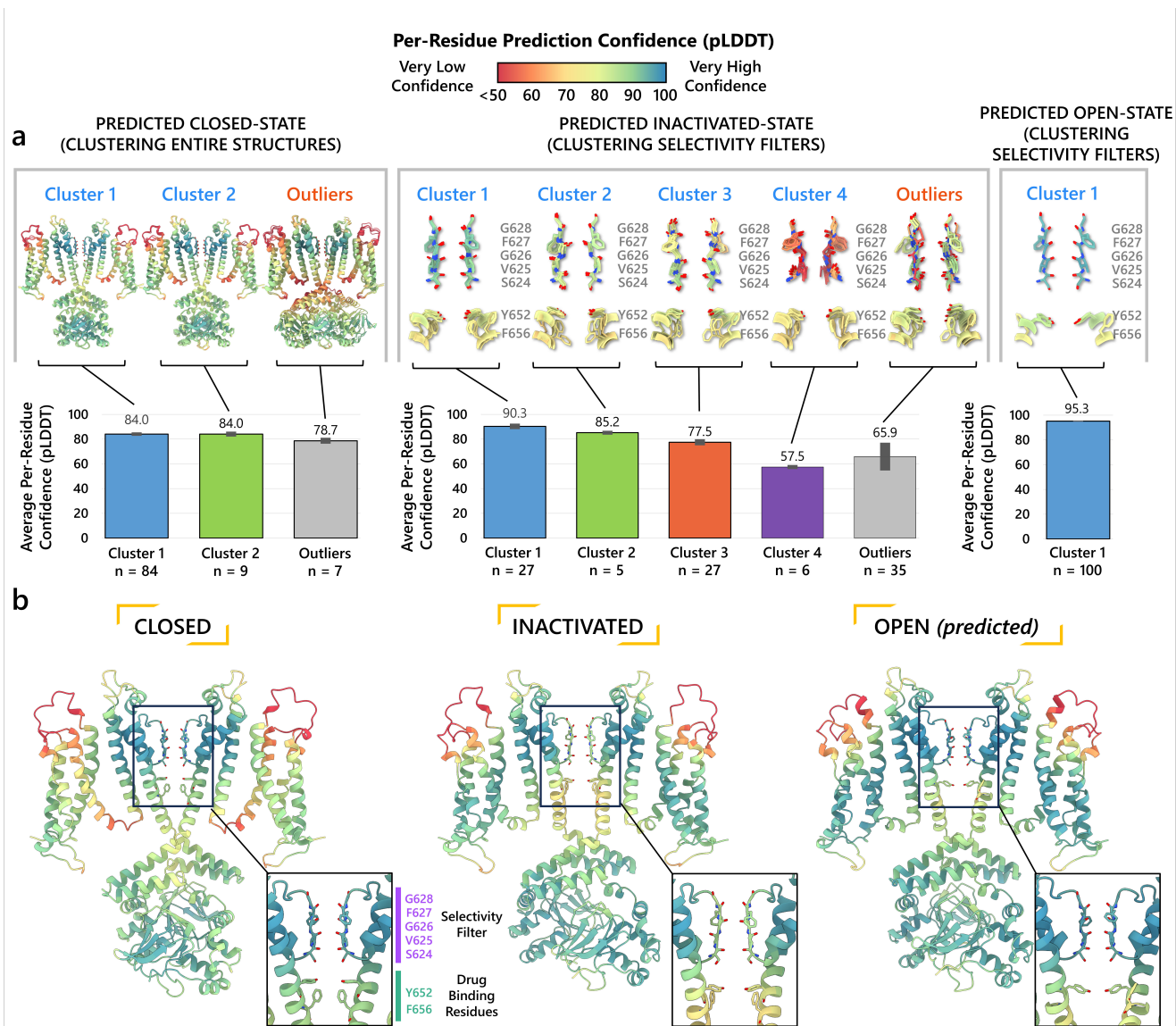
Figure 2. Clustering of AlphaFold2-predicted hERG channel models. a) Clusters created from 100 models predicted for each state. Each structure visualized is colored according to the per-residue confidence metric (pLDDT). The closed-state models are clustered based on the C-alpha RMSD of the entire protein models. The inactivated- and open-state models are clustered based on the all-atom RMSD of the selectivity filter (S624 – G628). To represent each cluster, the top 5 models ranked by average pLDDT are shown. The bar graphs display the mean pLDDT values for the clustered segment across all models within each cluster, accompanied by the standard deviation. Clusters containing less than three models are categorized as outliers. **b)** The models chosen for subsequent analysis**.**
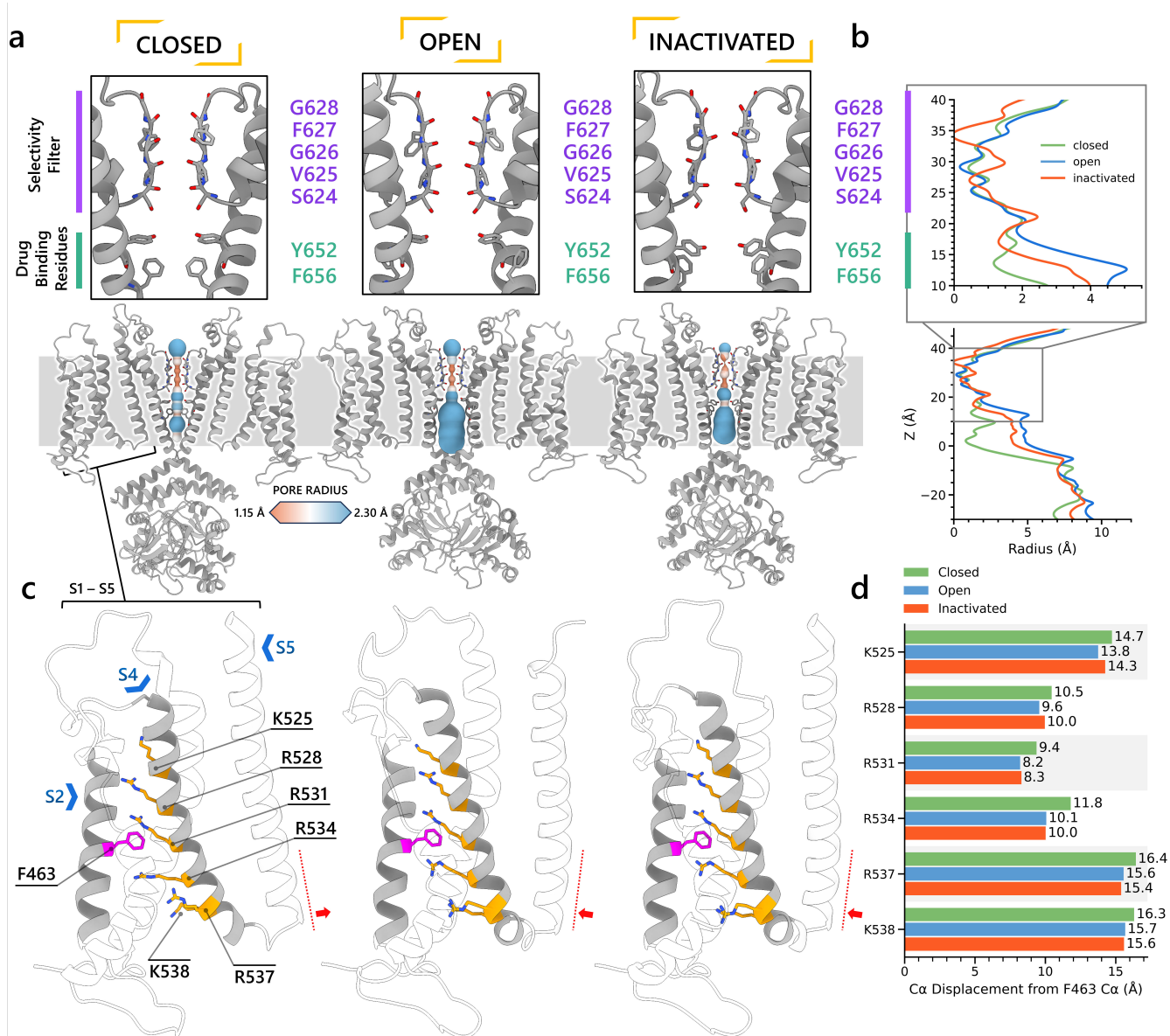
Figure 3. Structural comparison of different hERG channel state models. a) Visual comparison of the closed, open-, and inactivated-state models. **b)** Pore radius for the SF and drug binding region (upper) and for the entire pore (lower). **c)** Comparison of the VSD conformation in each model, showcasing the positively charged Arg and Lys gating-charge residues (yellow), located on the S4 helix, and the gating charge transfer center residue, F463 (magenta), on the S2 helix. **d)** Distances between the C_α atom of F463 to the C_α atom of each of the gating-charge residues.
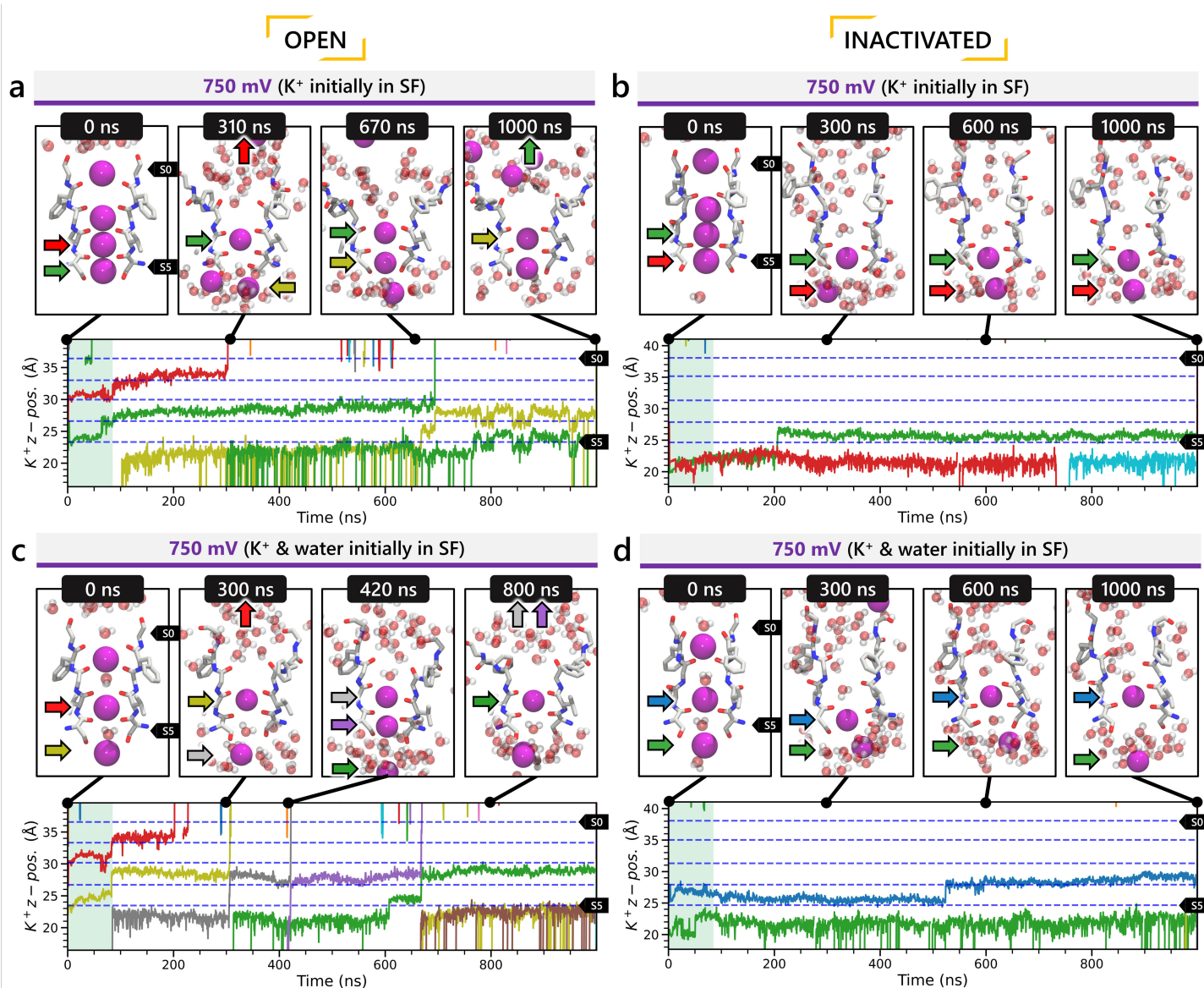
Figure 4. Movement of K⁺ ions through hERG SF. The z coordinates of K⁺ ions are tracked as they traverse the pore of the channel from the intracellular gate (lower y-axis limit) to the extracellular space (upper y-axis limit) under the membrane voltage of 750 mV. Putative K⁺ binding sites in the SF (S0 – S5) are marked using blue dashed lines in the plots. **a, c)** Results from MD simulations on the open-state model with the SF initially configured to have only K⁺ ions (panel **a**) or alternating K⁺ / water molecules (panel **c**), respectively. **b, d)** Results from MD simulations on the inactivated model with the SF initially configured to have only K⁺ ions (panel **b**) or alternating K⁺ / water molecules (panel **d**), respectively.
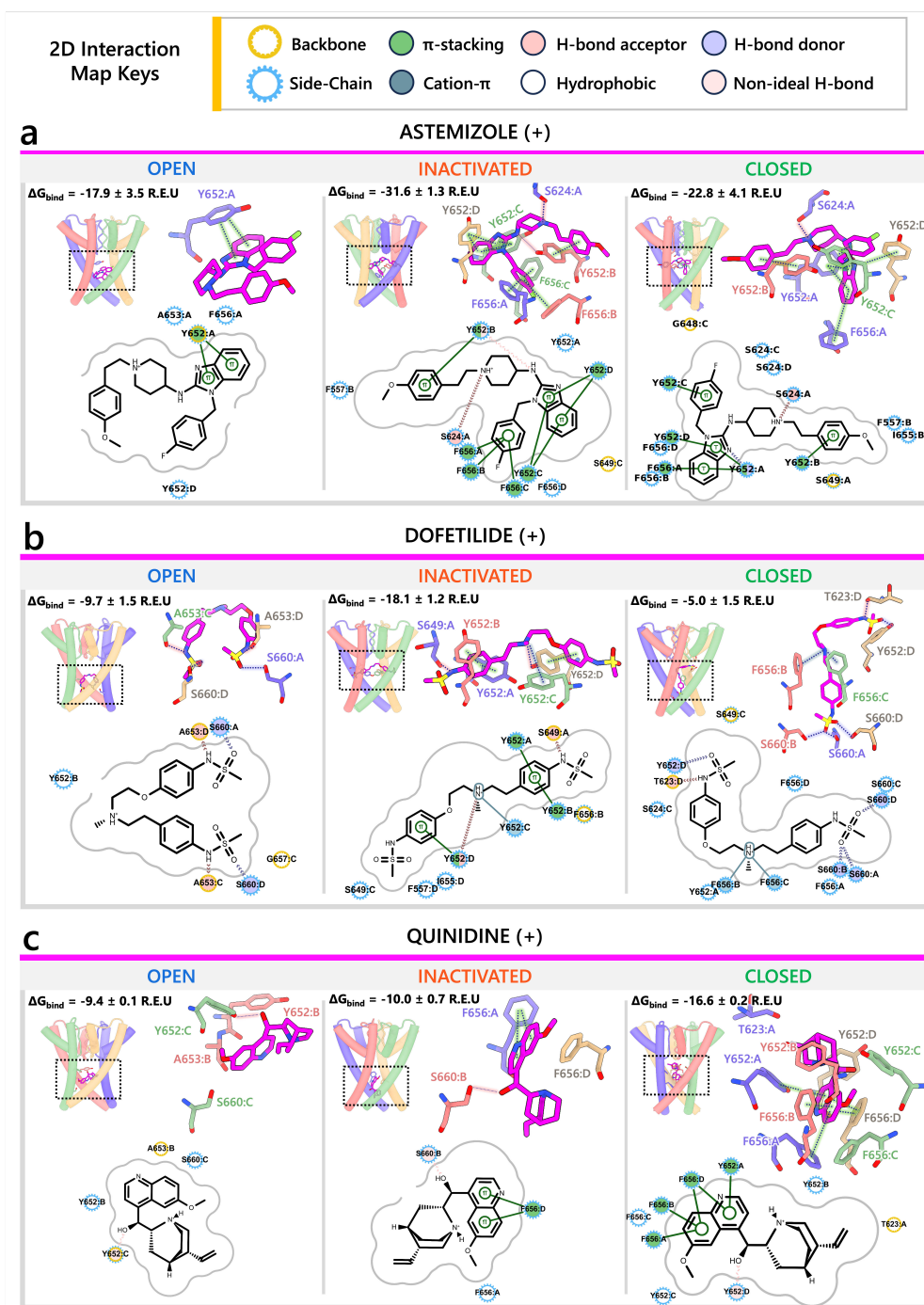
Figure 5. Visualization of interactions for cationic astemizole (a), dofetilide (b), and quinidine (c) with different hERG channel models. Each panel includes 3 subpanels showcasing drug interactions with the open-, inactivated, and closed-state hERG channel models. The estimated drug binding free energies, ΔG_{bind}, are given in Rosetta energy units (R.E.U). In each subpanel, an overview of where the drug binds within the channel pore is shown on the upper left, a 3D visualization of interactions between each channel residue (blue, red, green, and tan residues are from the subunit A, B, C, or D, respectively) to the drug (magenta) is shown on the upper right, and a 2D ligand – protein interaction map is shown at the bottom. A continuous gray line depicts the contour of the protein binding site, and any breaks in this line indicate areas where the ligand is exposed to the solvent.
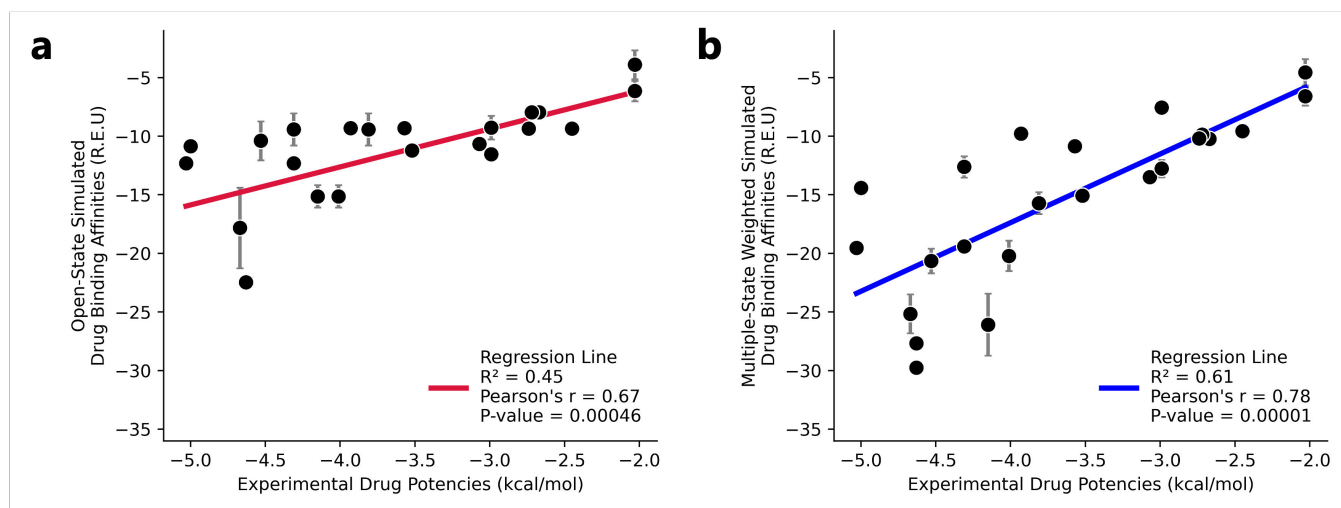
Figure 6. Correlation of predicted hERG drug binding affinities obtained from GALigandDock, in Rosetta Energy Units (R.E.U.), with experimental drug binding potencies (IC$_{50}$) converted to kcal/mol. Lower (more negative) binding energies indicate stronger binding. For each drug and hERG channel state, the top 50 out of 25,000 binding poses were clustered based on their root-mean-square deviations (RMSDs), and the average binding affinity from each cluster was used to represent the drug – ion channel interaction. **a)** A control scenario where only the open-state binding was considered, which is the conventional approach in ion channel pharmacology due to the lack of structural data for other states. **b)** A scenario that considers drug binding to different ion channel states (open, inactivated, and closed) predicted by our AlphaFold2 approach. The binding affinities for each hERG channel state were adjusted by the probability of that state occurring, based on a five-state model, and the drug's ionization state at the experimental pH and temperature. This enabled a more accurate comparison between the computational drug binding affinities and experimental IC$_{50}$ values, which were converted to kcal/mol. When accounting for drug binding to multiple channel states, the simulated binding affinities showed a 35.6% improvement in R² (0.61 vs. 0.45), a stronger correlation (Pearson's r = 0.78 vs. 0.67), and greater statistical significance (P-value = 0.00001 vs. 0.00046) compared to the conventional approach of considering only open-state binding. This suggests that even a simplified multi-state model offers better predictive power, with further improvements likely when drug-induced gating modulation is included in future studies.

Supplementary Figures
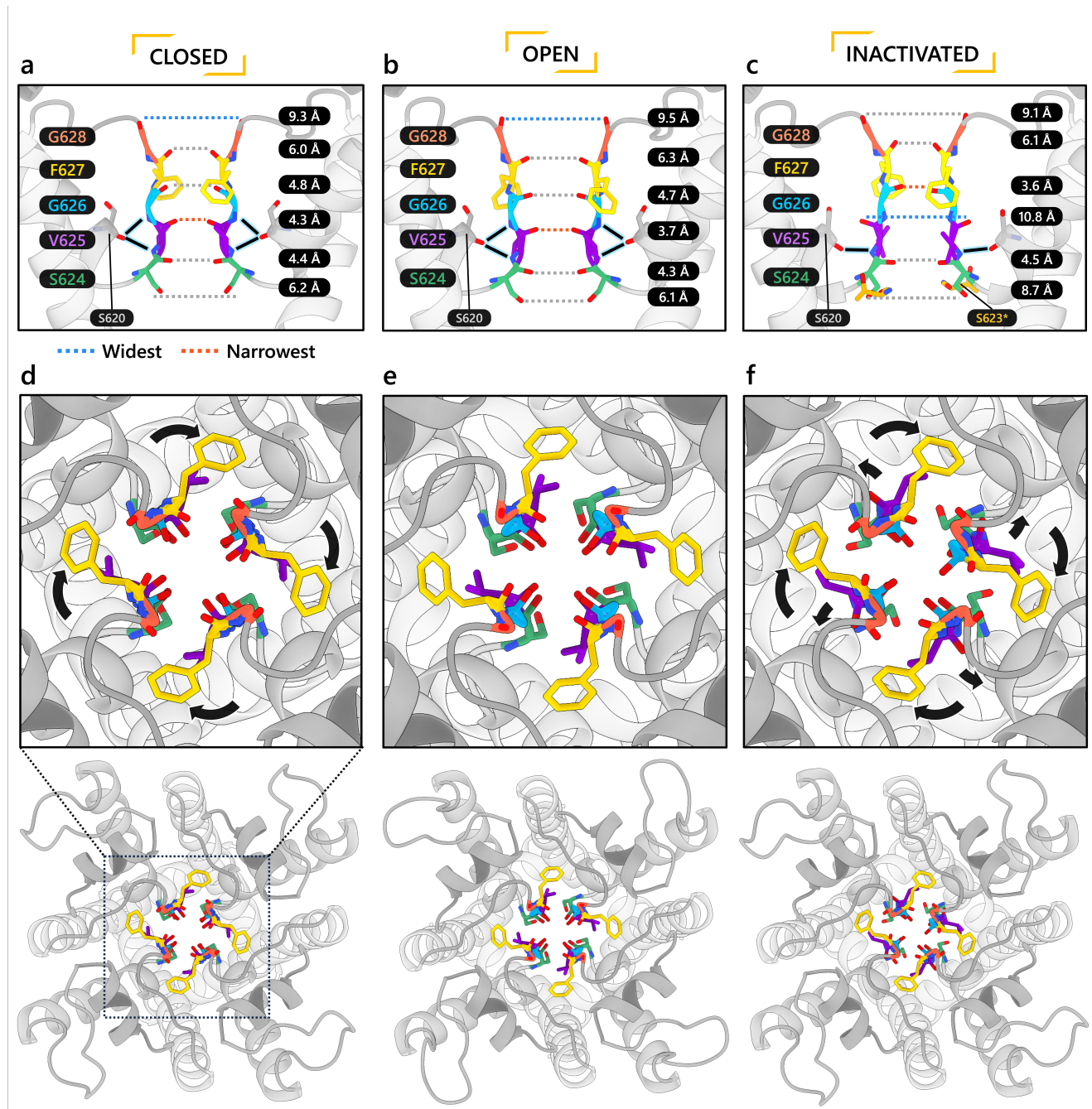
Figure S1. Comparison of the SF in hERG closed- (a, d), open- (b, e), and inactivated-state (c, f) models. a, b, c) Measurement of the distances between each carbonyl oxygen lining the conduction pathway in the SF. In the open- and closed-state models, S620 backbone carbonyl interacts with G626 and S624 backbone amide NH groups. In the inactivated-state model, the hydrogen bond between S620 and G626 is absent due to a reorientation of V625 backbone. However, at the bottom of the SF, S624 sidechain interacts with S623 backbone carbonyl from an adjacent subunit (denoted by *). **d, e, f)** View of the SF from the extracellular side. Large arrows indicate the rotation of the F627 side chains, while small arrows show the rotation of the loops that connect the upper SF to the S6 helix, all relative to the equivalent structural elements in the open-state model.

40
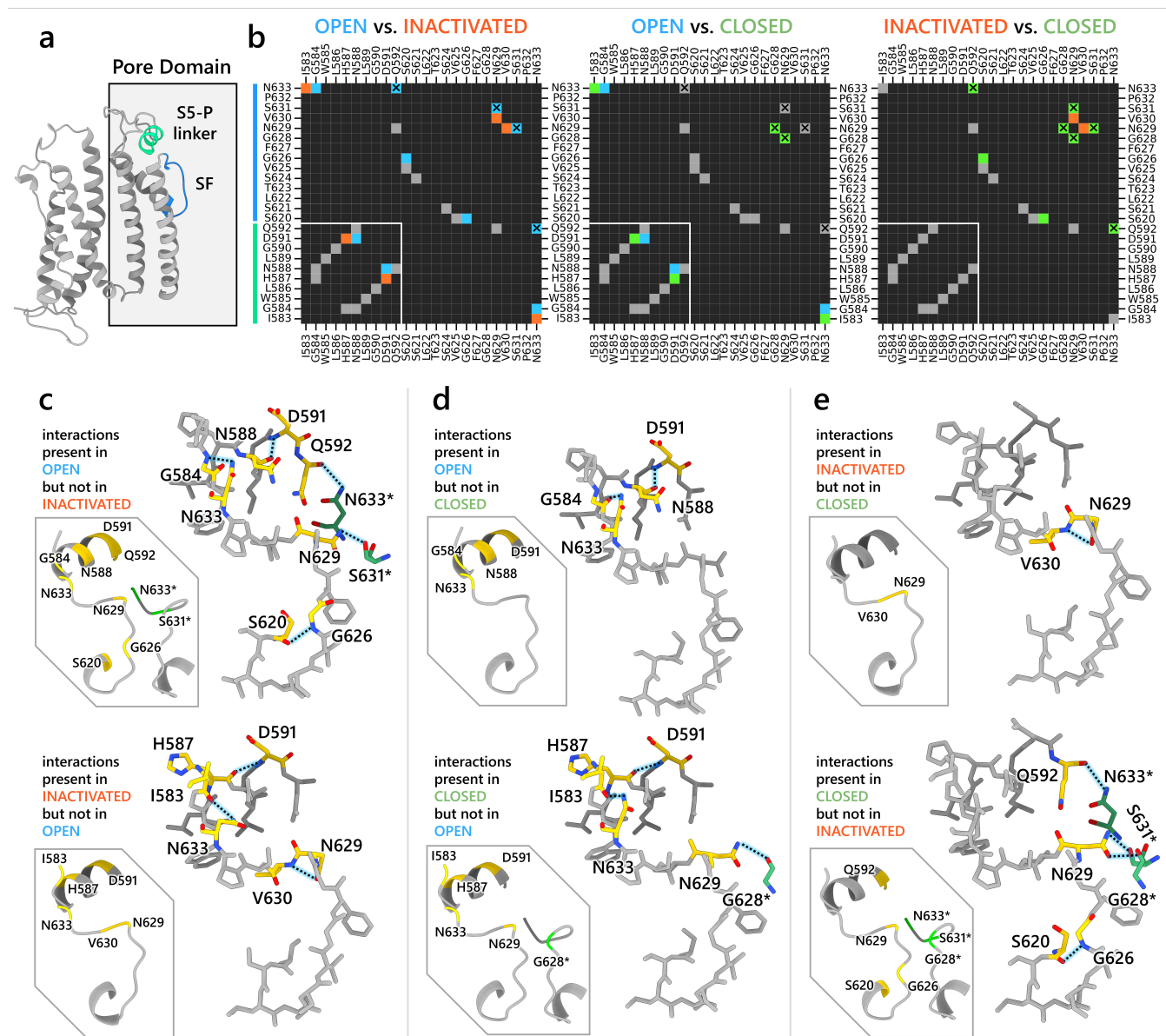
Figure S2. Interaction network analysis showcasing residue-residue interactions in the S5-P linker (I583 – Q592) and region surrounding the SF (S620 – N633). a) An image of a hERG channel subunit with the analyzed S5-P linker and SF regions colored in light green and light blue, respectively. **b)** Heatmaps showing intrasubunit and intersubunit (marked by X) interactions between each residue in the analyzed regions. The interactions analyzed are hydrogen bonding, π stacking, cation-π, and salt bridges. Black cells indicate no interactions. Gray cells indicate an interaction is present in both states. Blue, orange, and green colored cells indicate the interaction is present only in the open, inactivated, or closed state, respectively, but not in the other state being compared in the map. White lines are added to separate S5-P linker residues from the SF region residues. **c, d, e)** Visualization of the interactions being present in one state but not the other. Gold-colored residues are involved in the interactions. Green-colored residues, named with an asterisk at the end, are from an adjacent chain but are interacting with gold-colored residues. Dashed lines represent hydrogen bonds.

41

Figure S3. Distance-based contact maps comparing intra- and intersubunit contacts between each model. Two residues whose C_α atoms are within 6 Å of each other are considered to be in contact, provided there are no C_α atoms belonging to a third residue in between. Black cells indicate no contacts. Gray cells indicate a contact is present in both states being compared. Blue, orange, and green colored cells indicate the interaction is present only in the open, inactivated, or closed state, respectively, but not in the other state being compared in the map. Colored topology labels are included along the left and bottom edges of the maps showing the specific segments of the hERG channel to which the residues correspond.
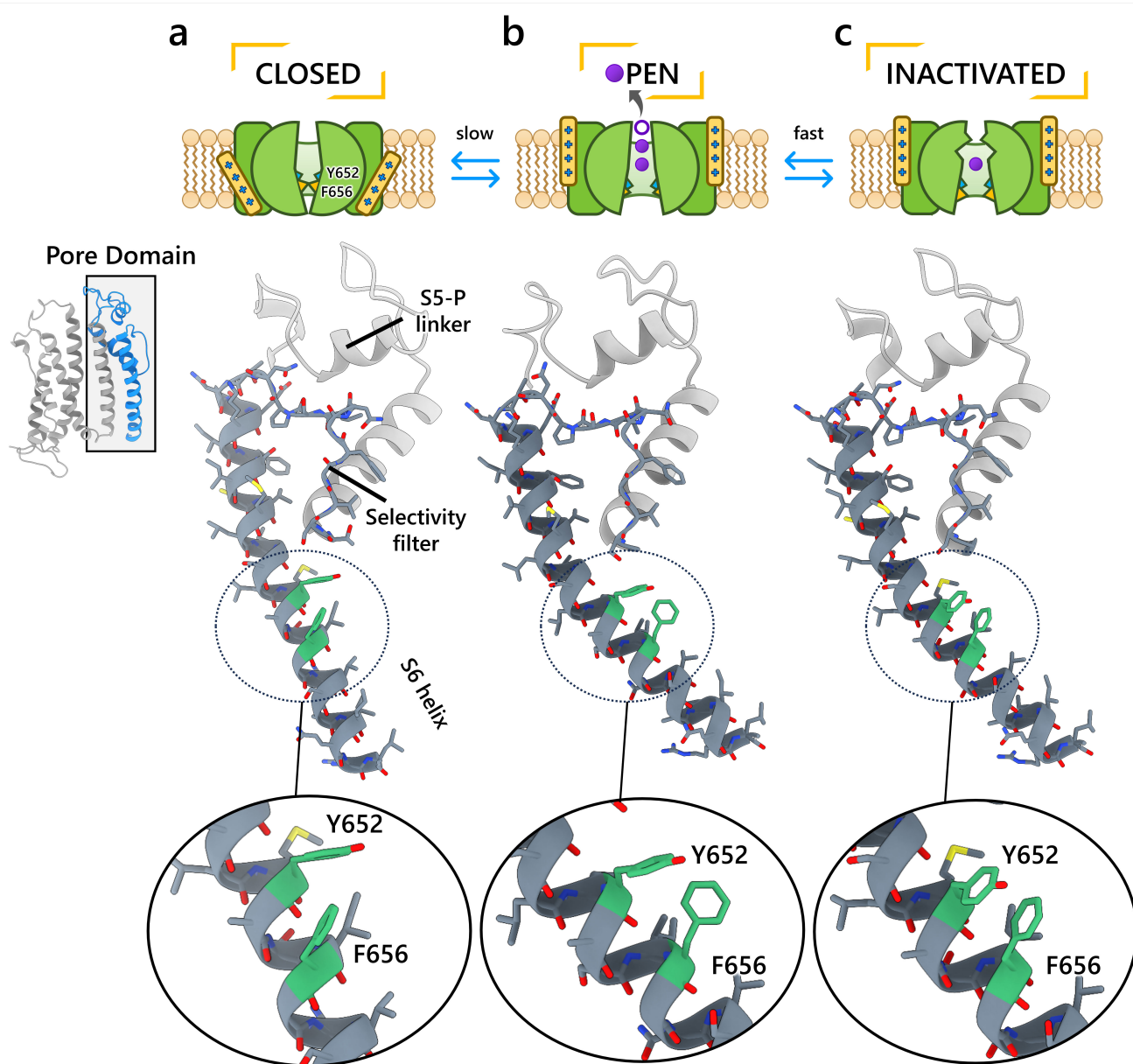
Figure S4. Comparison of the S6 helix conformation for the hERG closed- (a), open- (b), and inactivated-state (c) models. Residues E575 – L666 from the pore domain are visualized as dark gray ribbons. Selectivity filter (SF) residues and those on the S6 helix are shown with their backbone and side chains displayed as colored sticks. C atoms are gray, O are red, N are blue, S are yellow, H are not shown. The drug binding residues Y652 and F656 are highlighted in green.
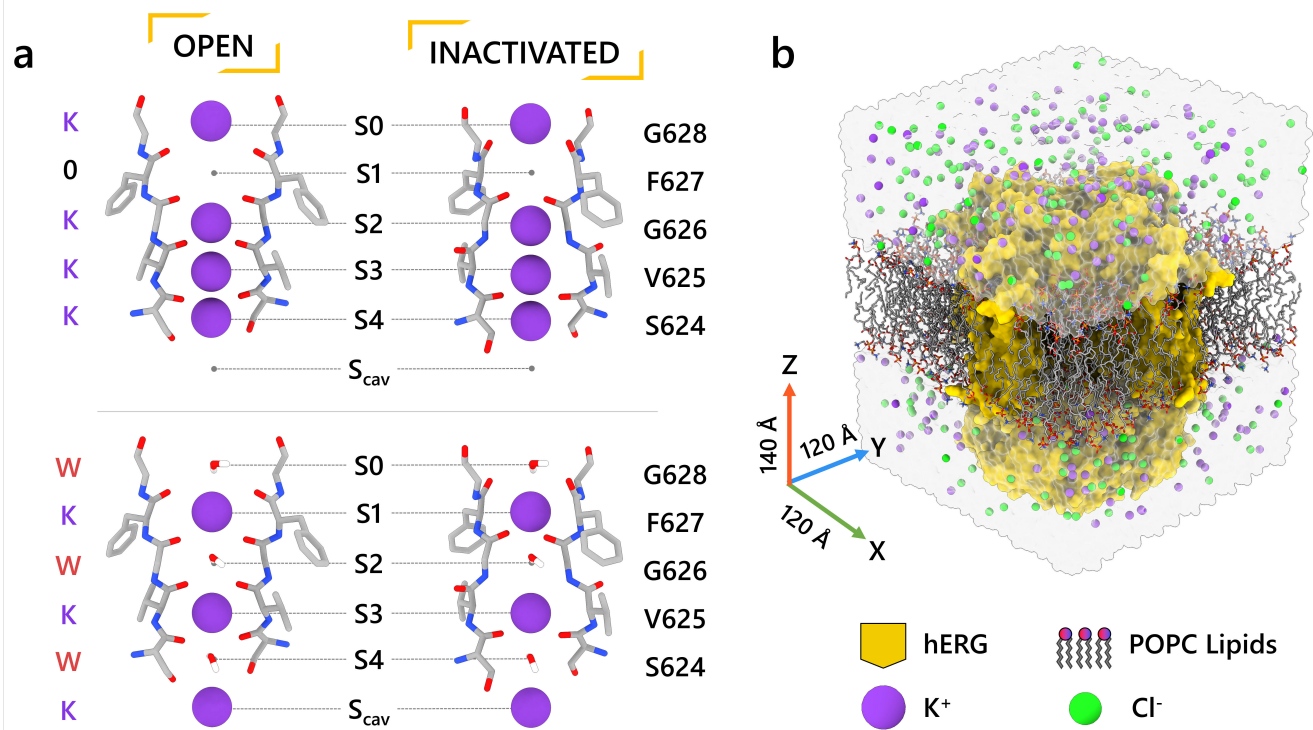
Figure S5. Setup of MD simulations to assess ion conduction in the open and inactivated hERG channel models. a) Initial configuration of the SF, set to fill with either all K^+ ions (top), or alternating K^+ and water molecules (bottom). **b)** An example MD simulation box showing a hERG channel model (shown in yellow surface representation) embedded in POPC lipid bilayer (shown as sticks) and solvated by an aqueous 0.3 M KCl solution (shown as a transparent surface with K^+ and Cl^- ions shown as purple and green balls, respectively).
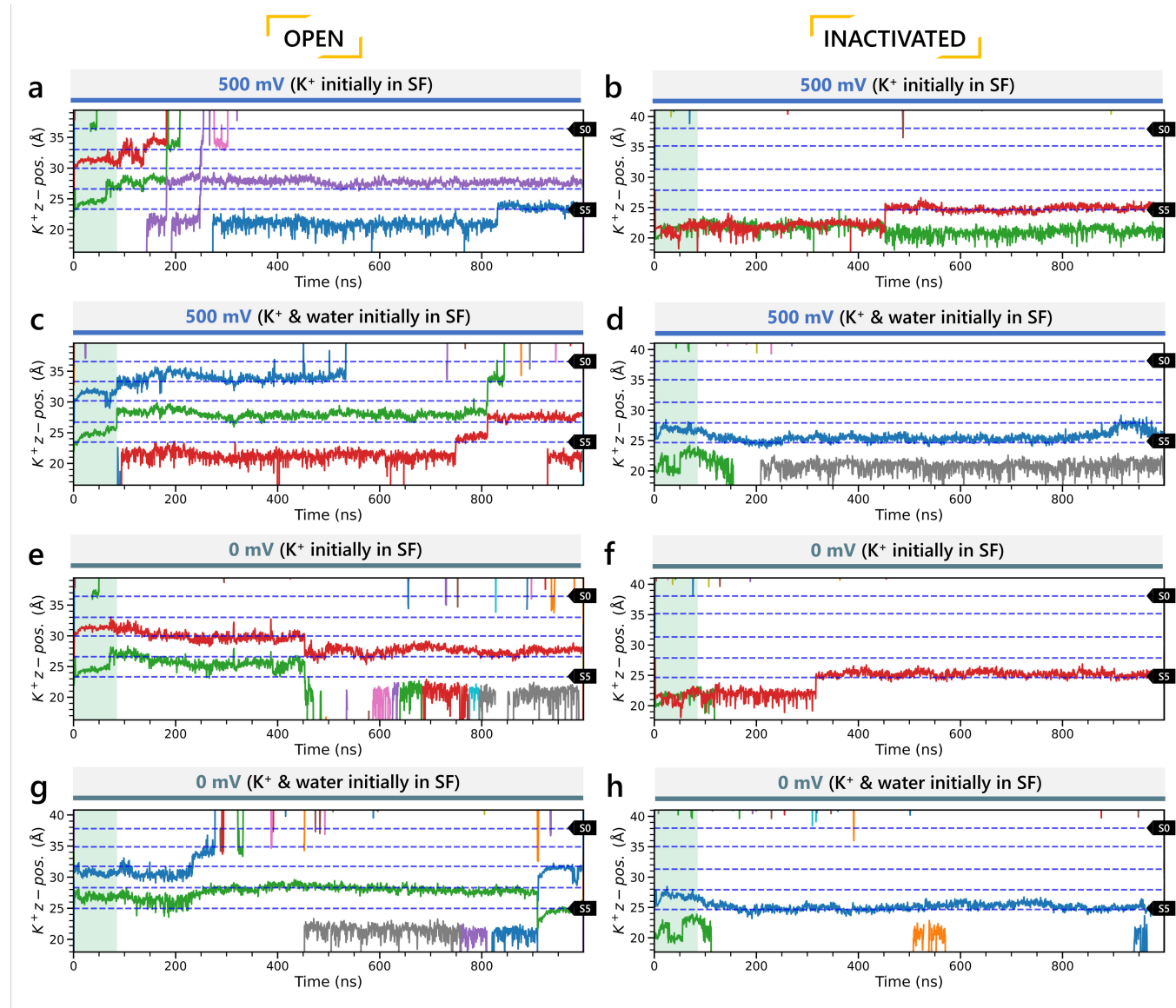
Figure S6. Movement of K⁺ ions through hERG selectivity filter (SF). The *z* coordinates of K⁺ ions are tracked as they traverse through the pore of the channel from the intracellular gate (lower *y*-axis limit) to the extracellular space (upper *y*-axis limit). Putative K⁺ binding sites in the SF (S0 – S5) are marked using blue dashed lines in the plots. **a, c)** Molecular dynamics (MD) simulations with the applied 500 mV membrane voltage of the open-state model with the SF initially configured to have only K⁺ ions (panel **a**) or alternating K⁺ / water molecules (panel **c**), respectively. **b, d)** MD simulations with the applied 500 mV membrane voltage of the inactivated-state model with the SF initially configured to have only K⁺ ions (panel **b**) or alternating K+ / water molecules (panel **d**), respectively. **e, g)** MD simulations without applied membrane voltage of the open-state model with the SF initially configured to have only K⁺ ions (panel **e**) or alternating K⁺ / water molecules (panel **g**), respectively. **f, h)** MD simulations without applied membrane voltage of the inactivated-state model with the SF initially configured to have only K⁺ ions (panel **f**) or alternating K⁺ / water molecules (panel **h**), respectively.
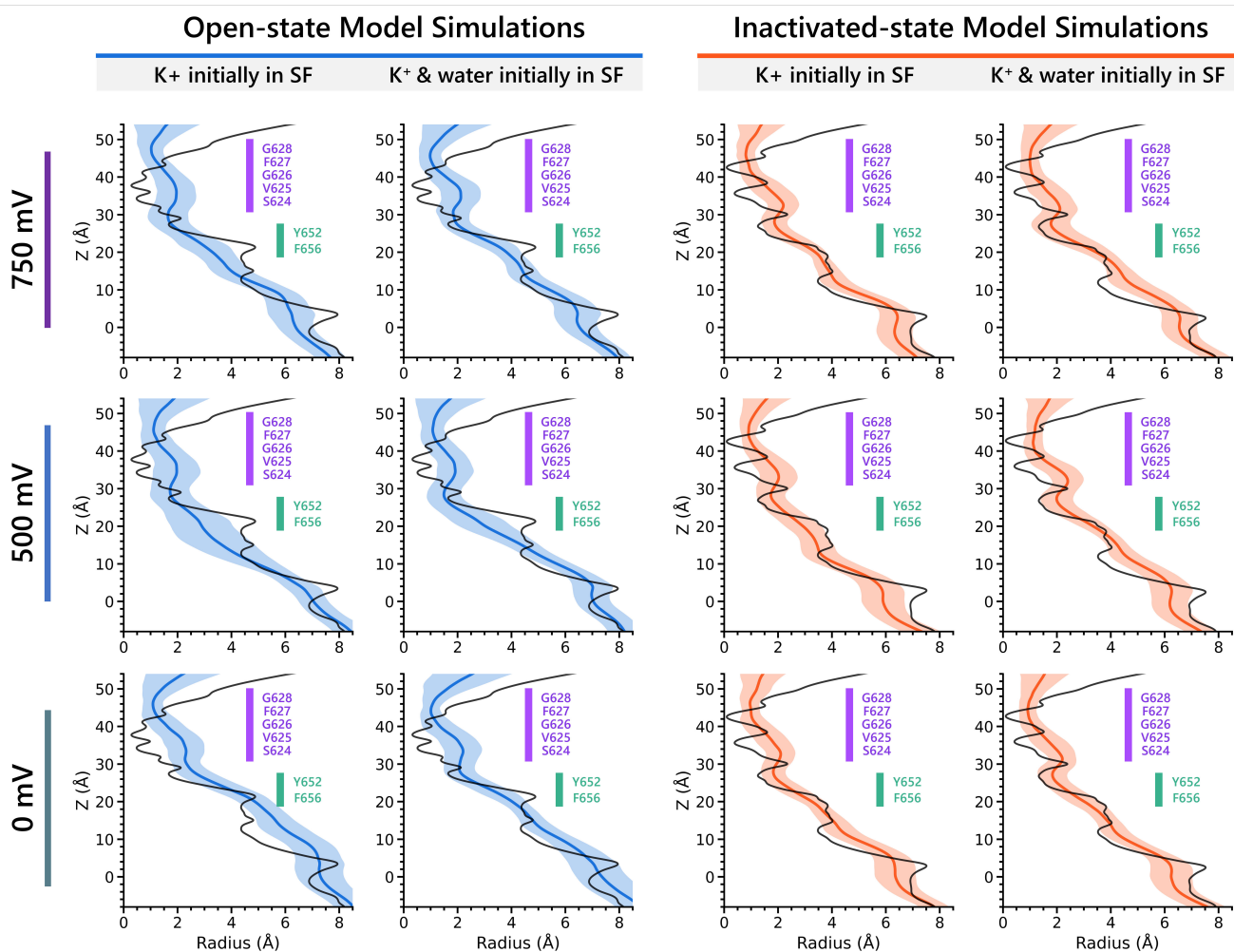
Figure S7. Analysis of modulations of the selectivity filter (SF) conformations and pore radii over the course of the 1 µs long molecular dynamics (MD) simulations. The blue/orange-colored lines represent the average pore radii, and the shaded regions represent the standard deviation measured in MD simulations for a given *Z* value. The black lines represent the initial pore radii. The label on the left indicates the voltage of the MD simulations in each row.
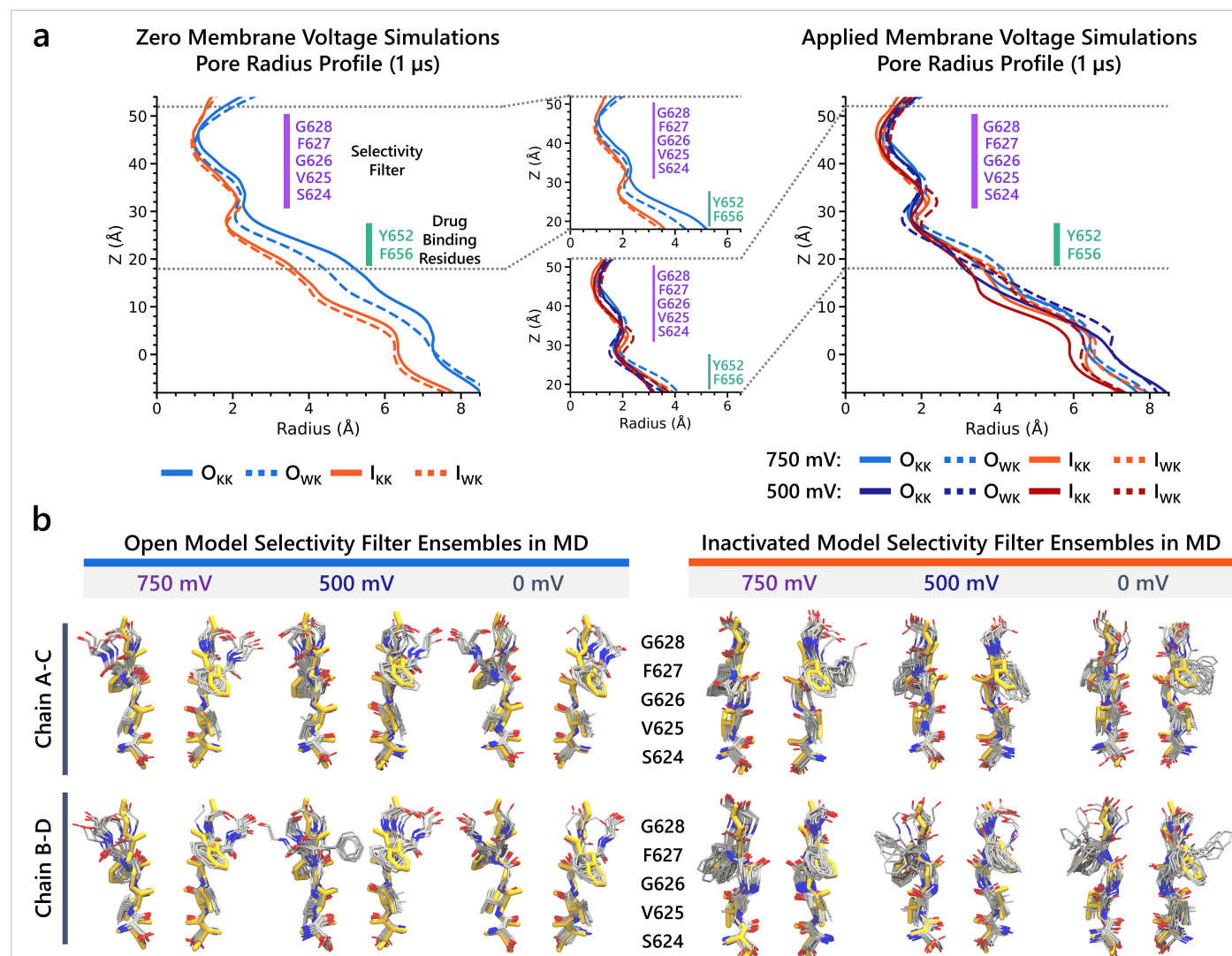
Figure S8. Analysis of dynamics of the SF and pore conformations over the course of the 1 μs MD simulations. a) Pore radius averaged over each 1 μs long MD simulations with (right) or without (left) applied membrane voltage. Open- and inactivated-state model MD simulations are notated as O and I, respectively, with the subscripts KK and WK denoting whether the SF initially configured to have only K^+ ions or alternating K^+ / water molecules, respectively. **b)** Ensembles of SF conformation over the course of each MD simulation superimposed. The golden-colored conformation indicates the initial conformation.
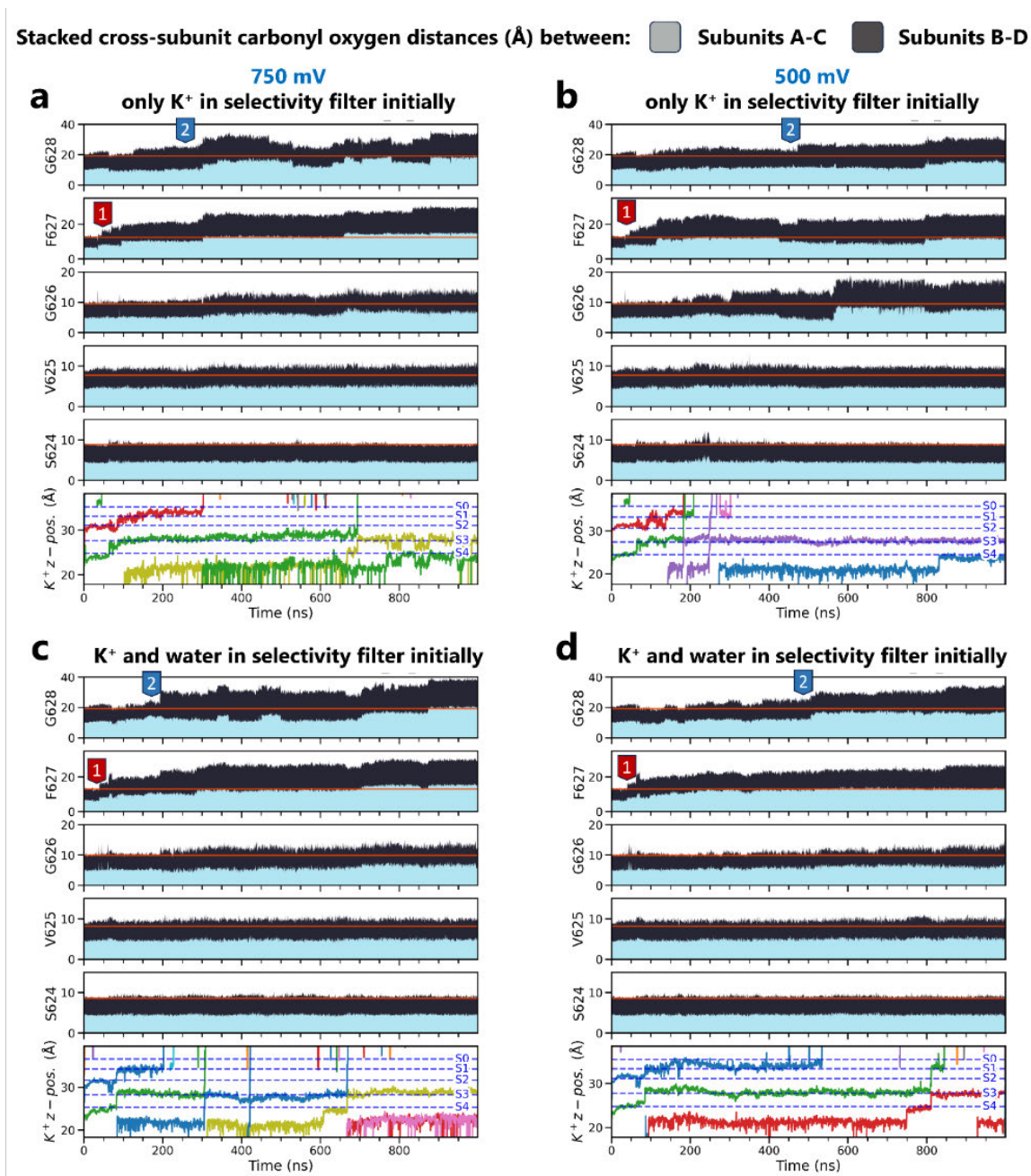
Figure S9. Cross-subunit distances between carbonyl oxygens of open-state hERG selectivity filter residues during MD simulations under different applied voltage and initial K⁺ ion position conditions. Movement of potassium ions (denoted by differently colored lines) is shown at the bottom for reference. Red lines indicate initial distances. Labels 1 and 2 in red and blue, respectively, indicate a sequential dilation process exhibited by the hERG channel: the SF near residues F627 dilates first, followed by that around G628.
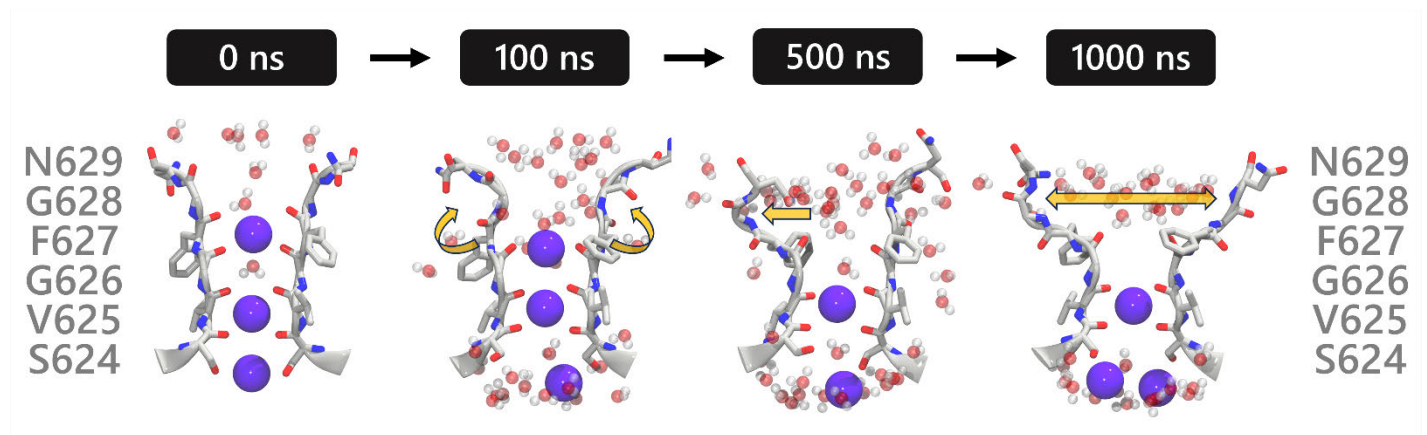
Figure S10. Sequential dilation steps of hERG upper selectivity filter (SF). SF residues are shown as gray sticks, water molecules as red and white spheres, and K^+ as purple spheres. The first step, occurring around 100 ns, involves the flipping of F627 carbonyl oxygen, creating a small dilation at this level. At 500 ns, further dilation can be seen at the level of residues F627 and G628 in one subunit. At 1000 ns, the entire upper region of the SF dilates further. Frames were taken from an MD simulation of the open-state hERG channel with K^+ and water initially in the SF prior to transmembrane voltage of 750 mV being applied.

Figure S11. GALigandDock drug docking results to different hERG channel models. Each bar plot represents the estimated free energy of binding in Rosetta energy units (R.E.U.) for the named drug to the open-, inactivated, and closed-state hERG channel models. Lower values mean more favorable binding. 25,000 docking poses were generated for each drug/channel model pairing. The top 50 poses were clustered, and the plotted energy represents the average free energy of the top cluster along with the standard deviation. The first suffixes (0), (+), and (±) indicate whether the drug is in the neutral, cationic, or zwitterionic form, respectively. The second suffixes * and † indicate validation from experimental studies (Alexandrou et al., 2006; Numaguchi et al., 2000; Perrin et al., 2008; Wang et al., 1997) showing whether the drug prefers binding to hERG inactivated state (*) or does not (†), respectively.

Movie S1 (separate file). Animation depicting the hERG channel transitioning through various states, beginning in the open state and ending in the closed state using the structural models developed in this study.

50